Dynamic Deployment of a Mini-tab for Aerodynamic Load Control

D. J. Heathcote[1]

Georgia Institute of Technology, Atlanta, Georgia, 30332-0405

I. Gursul[2], **D. J. Cleaver**[3]

University of Bath, Bath, England, BA2 7AY

Load control is the reduction of extreme aerodynamic forces produced by gusts, maneuvers and turbulence, to enable lighter, more efficient aircraft. To design an effective control system the actuator's response, in terms of amplitude and phase lag, must be known. Current load control technologies are limited to low frequency disturbances due to their large inertia. This paper evaluates a potential high frequency alternative: the mini-tab using periodic and transient deployments on a NACA0012 airfoil in wind tunnel experiments. Periodic deployment for reduced frequencies, $k \leq 0.79$ exhibits a normalized lift response amplitude which decays with increasing k comparable to Theodorsen's circulation function, but with substantially higher lag. Transient deployment, at rates as low as $\tau_{deploy} = U_\infty t_{deploy}/c = 1$, illustrated a delay in aerodynamic response. The delay is larger for outward mini-tab motion than inward, $\tau \approx 6$ and 4 respectively for $\alpha = 0°$ and increases with α. The flowfields show that the delay in response and reduction in effectiveness for dynamic mini-tab deployment is due to delayed growth of the separated region behind the mini-tab. The aerodynamic response due to mini-tab deployment was approximated as the response of a first order system, pertinent to control system design. This simple characterization for amplitude reduction and delay in response makes it well suited to loads control.

---

[1] Postdoctoral Fellow, George W. Woodruff School of Mechanical Engineering, Member AIAA.

[2] Professor, Department of Mechanical Engineering, Associate Fellow AIAA.

[3] Senior Lecturer, Department of Mechanical Engineering, Member AIAA.

Nomenclature

α = angle of attack

a = speed of sound

AR = force calibration amplitude ratio

b = span

c = airfoil chord length

c_l = time-averaged lift coefficient, $L/(0.5\rho U_\infty^2 bc)$

$c_{l,\,h=0}$ = time-averaged lift coefficient for $h = 0$

$c_{l,hmax}$ = time-averaged lift coefficient for h_{max}

$c_{l,max}$ = maximum phase-averaged lift coefficient

$c_{l,min}$ = minimum phase-averaged lift coefficient

$\Delta c_{l,s}$ = change in lift coefficient from baseline, static, $c_{l,hmax} - c_{l,\,h=0}$

$\Delta c_l(t)$ = change in lift coefficient from baseline, time dependent, $c_l(t) - c_{l,\,h=0}$

f = actuation or gust frequency

h = mini-tab height

h_{max} = maximum mini-tab height

k = reduced frequency, $\pi fc/U_\infty$

κ = non-dimensional time constant for first order system

Ma = Mach number, U_∞/a

U_∞ = free-stream velocity

ρ = fluid density

Re = Reynolds number, $\rho U_\infty c/\mu$

t = time

t_{deploy} = deployment period

T = Period of mini-tab deployment

τ = Non-dimensional or convective time unit, $U_\infty t/c$

τ_{deploy} = Non-dimensional transient deployment period, $U_\infty t_{deploy}/c$

θ = calibration phase angle

u = streamwise velocity component

v = cross-stream velocity component

μ = dynamic viscosity

x = chordwise location

x_f = mini-tab chordwise location

y = position perpendicular to free-stream

z = spanwise location

1. Introduction

In recent years, aerodynamic load control, through both active and passive means, has become a nascent area of research. It aims to control the increased aerodynamic loads experienced during gusts, turbulence and maneuvers, to reduce those passed to the aircraft structure. These events are typically short in period but can be severe. A maximum reduced frequency in the range k = 0.75 to 1 is obtained for an aircraft at cruise if the gust profile is considered as sinusoidal [1].

Current aerodynamic loads alleviation actuators, such as ailerons, flaps and spoilers, have a large inertia and are unable to control higher frequency loads. An aerodynamic load control device with an improved frequency response could reduce the structural requirement, lower aircraft weight and allow for a greater payload, lower emissions and a longer aircraft range while improving passenger comfort. To design an effective control system, the aerodynamic response of the actuator must be characterized.

The mini-tab, a small span-wise strip placed normal to the upper surface of the airfoil, has been proposed as a possible solution. Previous results [2, 3] indicate that the mini-tab is effective at reducing lift in a static configuration. The mini-tab separates the flow over a portion of the airfoil surface, providing an effect which is highly dependent on mini-tab height, h/c, chordwise location, x_f/c and the airfoil's angle of attack, α. For a normalized height, h/c = 0.02, mini-tab placement close to the trailing edge has decreasing effect with increasing angle of attack towards stall, as the baseline flow separation engulfs the mini-tab. Utilization close to the mid-chord (x_f/c = 0.60) produces a large lift reduction across a wide range of angles of attack (α = 0 to 5°) with a steady state change in lift coefficient, $\Delta c_{l,s}$ of up to -0.60 for a mini-tab of height, h/c = 0.04. As with placement near the trailing edge, the effectiveness of mid-chord placement reduces towards stall. Placement close to the leading edge (x_f /c = 0.08) efficiently separates the flow at low incidences with little change in lift due to flow reattachment, however, with increasing angle of attack a corresponding increase in lift reduction is observed with $\Delta c_{l,s}$ ≈ -0.68 feasible for h/c = 0.04.

While these measurements indicate the mini-tab's promise in a static configuration, dynamic actuation determines the mini-tab's efficacy as a high frequency load control actuator. This paper examines a dynamically deployable mini-tab and its effect on time variant lift. The response is assessed using periodic and transient mini-tab motions. The literature associated with these two scenarios is presented in Sections 1.1 and 1.2.

1.1 Periodic Mini-tab Deployment

Periodic mini-tab deployment refers to a cyclic, typically sinusoidal, motion that is used to determine the aerodynamic frequency response in terms of amplitude and phase angle. The deployment frequency is expressed as a reduced frequency, k. Periodically deployed mini-tabs have been considered for lift augmentation on a retreating rotor blade [4, 5], flutter suppression on highly flexible wings [6, 7] and wind turbine load mitigation [8].

Whether the mini-tab provides lift increase or decrease depends on the deployment surface: placement on the lower surface produces lift increase. Placement on the upper surface produces lift decrease: the aim of this study. A comparison [3] of literature for static mini-tab measurements indicates that around the airfoil's zero lift angle the mini-tab's effect on the flow is symmetrically similar for upper and lower surface placement. As such, the effect of periodically deployed mini-tabs on the upper and lower surfaces will be considered concurrently.

Periodic mini-tab deployment through a circular arc at $x_f/c = 0.70$ for reduced frequencies, $k \leq 0.92$ was investigated by Clevenson & Tomassoni [9]. The peak-to-peak change in lift, $(c_{lmax} - c_{lmin})$ decreased as k increased. A significant delay in response was indicated by a large phase angle of up to $\varphi = 125°$ for the lowest Reynolds number tested ($Re = 1.3\text{x}10^6$). Computations [5, 10] produced similar results, however the study of Tang & Dowell [11] indicated an increase in $(c_{lmax} - c_{lmin})$ as k increases but with the same delay.

Kinzel *et al* [10] normalized the peak-to-peak change in lift by the static value, i.e., $(c_{lmax} - c_{lmin})/\Delta c_{l,s}$. The resulting trend was comparable to the reduction in amplitude obtained by Theodorsen's function [12]. This is surprising given Theodorsen's function was first developed for pitching and plunging airfoils with fully attached flow and therefore does not model non-linearities in the flow-field, such as vortex sheet roll-up and flow separation (as produced behind the mini-tab). Similar trends were noted by Lee & Kroo [7].

The time dependent change in lift, $\Delta c_l(t)$ is a function of the mini-tab deployment height, $h(t)$. It was noted by [10, 11] that a hysteresis loop develops as k increases, indicative of a delay in aerodynamic response. Some numerical studies [4, 13] also note an adverse effect (opposing the desired change in lift) during the outward phase that was attributed to the growth of a vortex behind the mini-tab. Once the vortex reaches the trailing edge, the lift progresses towards the desired value.

Clevenson & Tomassoni [9] used Schlieren photography to examine the flowfield produced by an oscillating mini-tab. Similar to static deployment, the mini-tab initiates a flow separation. For the same mini-tab height a larger separation region was observed during the inward than the outward phase of motion, indicating delay in aerodynamic response.

Within the literature there is clear evidence that the mini-tab's efficacy, in terms of amplitude and phase, decays with increasing reduced frequency. However, this information is spread over many studies with very varied experimental parameters: $0.2 \leq Ma \leq 0.6$, placement on upper / lower surface, different locations from $x_f/c = 0.7$ to 1 and different airfoil profiles, resulting in varied magnitudes of amplitude decay and phase delay. While the effect of angle of attack has been evaluated numerically, such as in the study of Liu et al [14], the effect has not been evaluated experimentally over a wide range of angles, and deployment reduced frequencies. It should be noted that the current study considers a much wider range of angles (from zero lift to stall), and a wider range of deployment reduced frequencies.

1.2 Transient Mini-tab Deployment

Transient deployment is particularly relevant to gust load alleviation. The mini-tab could be deployed at the beginning of a gust and held in position until it has subsided, reducing lift and thus the peak aerodynamic loads. Chow & Van Dam [15] evaluated the lift response of transient mini-tab deployment and its effect on the wider flowfield using RANS CFD. A vortical structure behind the mini-tab was observed, which initially produced an adverse response. The vortex grows as the mini-tab is deployed eventually reaching the trailing edge. The lift response then begins to progress towards the static, final value. Coder *et al* [16] suggested that the adverse effect was reduced by increasing the deployment period, τ_{deploy}. Vieira & Maughmer [13] used an empirical method, modelling the effect of the vortex and circulatory forces on lift separately, obtaining similar results.

Bach [17] experimentally explored the effect of the non-dimensional deployment period, τ_{deploy}. A slow deployment (τ_{deploy} = 31.7) incurred minimal delay in lift response, whereas a fast (τ_{deploy} = 3.2) deployment produced a large lag with the lift response only attaining the final static value at $\tau \approx 10$. An inward deployment direction produced a larger lag in response than outward deployment.

While the adverse effect due to the vortex progression has been found widely with computational studies, experimental measurements [17-19] do not observe the vortical structure, with no adverse lift response. Comparing the testing conditions, the computational studies consider deployment periods as low as τ_{deploy} = 1, while experimental studies have considered deployment periods down to τ_{deploy} = 3.2. Therefore, there exists a need to experimentally investigate the transient behavior of the mini-tab at lower values of τ_{deploy} of the order 1. The experimental study here aims to address this gap between numerical simulations and experimental studies.

1.3 Aims and Objectives

The present study aims to address many of the gaps in the literature through a comprehensive experimental study of the dynamically deployed mini-tab including periodic and transient mini-tab motions. The effects of mini-tab deployment amplitude, h_{max}/c, reduced frequency, k and airfoil angle of attack, α will be simultaneously investigated. For periodic motion, the frequency response will be characterized by the change in lift reduction amplitude and phase angle as a function of actuation reduced frequency. For transient motion, the temporal response will consider the time delay between mini-tab actuation and the lift response. Phase-locked Particle Image Velocimetry measurements will elucidate the effects of periodic and transient mini-tab motion on the surrounding flowfield . Finally, the mini-tab lift response will be approximated as a first order system, to aid load control system design.

2. Experimental Apparatus & Procedures

2.1 Experimental Set-up

Experiments were conducted in the University of Bath's closed-return wind tunnel, which has a working section of 2.13 x 1.51 x 2.70 m with an octagonal cross-section. The free-stream velocity, U_∞ = 20 ms^{-1} for all tests with a turbulent intensity less than 0.5%. Figure 1(a) illustrates the working section, with the airfoil model shown *in-situ*. A NACA0012 profile model was used with a chord length, c = 0.5 m and span, b =1.5 m. The profile was used due to its symmetric nature and the wide range of literature data available. The span enabled the wing to traverse the wind tunnel cross-section with a small clearance at either end of 5 mm or 0.3%b. This avoided physical interference with the wind tunnel walls and minimized three dimensional effects by using the wind tunnel walls as end plates. A trip wire was used to promote boundary layer transition, placed at the location of maximum velocity, as suggested by Barlow *et al* [20]. A wire of diameter 0.3 mm was sized using the methods of Pankhurst & Holder [21] and was placed at a chord-wise location, x/c = 0.10. The lift curve (c_l-α) produced by this set up was previously [1, 3] compared to data in literature [22], with similar results obtained for a comparable Reynolds number. The interference and blockage effects were quantified using the methods of Pankhurst & Holder [21], and were determined to have minimal effect [1]. Reynolds number, *Re* was 6.6x10^5 for all tests.

The wing was constructed in two parts (see Fig. 1(a)). The initial 0.725c was constructed from carbon fiber composite with an aluminum support structure to create a rigid yet light wing. The final 0.275c was constructed from selective laser sintered (SLS) Nylon in five 0.3 m sections, allowing for the actuation method (mini-tab or jet flap [23]) near the trailing edge to be changed.

Placement near the trailing edge is desirable for small angles of attack, such as those encountered by an aircraft at cruise. The mini-tab's chord-wise location, x_f/c = 0.85 was selected as it provides sufficient internal volume for the mini-tab to be fully retracted within the trailing edge, while achieving a maximum deployment height, h_{max}/c = 0.015. Previous measurements [3] have shown that the static lift reduction produced by a mini-tab at x_f/c = 0.85 is similar to that at x_f/c = 0.95. For a mini-tab height of h/c = 0.02, the change in lift was identical for both locations (Δc_l = -0.29); whereas for a mini-tab height of h/c = 0.04 the change in lift was very similar for both locations: Δc_l = -0.46 and -0.42.

The mini-tab was constructed from 3 mm thick acrylic and was 1475 mm long, producing a small gap at either end (0.8%b) to avoid interference with the wind tunnel walls. An ideal, linear mini-tab deployment profile was not achievable due to the size constraints. The mini-tab moved through an arc (see Fig. 1(b)), supported by two rotational elements per section. The mini-tab was not normal to the airfoil surface for the full range of motion, with a difference of 13° between h/c = 0 and h/c = 0.015. Li *et al* [24] indicated that this angle's effect is small.

The mini-tab actuation mechanism is shown in Figs. 1(b) and (c). The design is similar to Tsai *et al* [25] but uses a sliding linkage rather than a pinned, 4 bar linkage mechanism. Each trailing edge section contains the same set up, ensuring that the mini-tab is uniformly actuated.

2.2 Dynamic Deployment

A closed-loop PID controller accurately executes the desired periodic and transient profiles. The position demand was provided by a National Instruments cRIO system and feedback of the mini-tab's position was provided by an optical linear encoder.

Periodic motion involves a sinusoidally oscillating mini-tab whose amplitude of oscillation is defined between the fully stowed condition ($h/c = 0$) and a defined maximum mini-tab height, h_{max}. This motion is described by equation 1. A maximum deployment error less than 5% was achieved.

$$\frac{h(t)}{h_{max}} = 0.5(1 - \cos 2\pi ft) \tag{1}$$

The actuation frequency is expressed in the form of a reduced frequency:

$$k = \frac{\pi fc}{U_\infty} \tag{2}$$

For the transient motion, the mini-tab is held at an initial position, $h_{initial}$ and then moved through a sinusoidal-step profile to the final position, h_{final}. For outward deployment $h_{initial} = 0$ and $h_{final} = h_{max}$; inward deployment is the inverse. The motion is described in equation 3, where t_{deploy} is the deployment period.

$$\begin{aligned} h(t) &= h_{initial} && t \le t_{deploy} \\ h(t) &= h_{initial} + 0.5(h_{final} - h_{initial})\left(1 - \cos\frac{\pi t}{t_{deploy}}\right) && 0 < t \le t_{deploy} \\ h(t) &= h_{final} && t > t_{deploy} \end{aligned} \tag{3}$$

The deployment period is normally expressed as a non-dimensional value:

$$\tau_{deploy} = \frac{U_\infty t_{deploy}}{c} \tag{4}$$

2.3 Force Measurements

The wing was mounted in the test section from above through an innovative force balance design (see Fig. 2(a)). Frictionless air bearings were aligned parallel to the lift force vector (y-axis) and supported the wing and force balance carriage. The air bearings remove any bending moment to leave pure lift force. The lift load was transmitted from the wing-carriage assembly through a FUTEK S-type force transducer. The design has been employed at a smaller scale to measure the dynamic lift force produced by a plunging airfoil [26]. The air bearing carriage includes an integrated rotary encoder with a measurement accuracy of ± 0.02° to control the angle of attack, α.

The force transducer signal was conditioned and acquired using a National Instruments cRIO, which also provided the position demand and measured the mini-tab's position. The signals were acquired concurrently at 5 kHz to allow calculation of any aerodynamic or mechanical system delay. The mini-tab's position was acquired as a quadrature signal at 50 kHz; the high acquisition frequency was required due to the mini-tab's high peak velocity.

Before each set of experiments, a static calibration was performed in order to find a force-voltage gradient and constant via a linear regression. For the calibration a minimum of ten discrete forces between 0 and 150 N were applied. In addition, the force balance dynamic response was assessed. The comparison method of Kumme [27] was used to determine a transfer function, in terms of amplitude ratio, AR and phase angle, θ between an input, known force and the output, unknown force balance signal. This allowed for any system resonant modes to be accounted and corrected for.

The experiment used an electromechanical shaker to provide a sinusoidal excitation to the wing. This force was monitored by an in-line FUTEK force transducer. The input force and signal from the air bearing force balance were phase-averaged over 100 cycles, with the excitation frequency varied between 0.5 and 20 Hz (k = 0.04 to 1.57). The peak-to-peak magnitude of the input force was varied between ±10 N, ±25 N and ±50 N to analyze the effect of input force amplitude on the force balance dynamic response.

Post processing was completed using MATLAB. The raw lift signal was first converted using a Fast Fourier Transform (FFT) to the frequency domain allowing for the effects of resonance to be corrected for via the use of the dynamic force balance calibration. The amplitude and the phase angle of the aerodynamic force measurements were calculated as the magnitude and angle between the real and imaginary components. The dynamic force calibration was then applied to correct the raw signal across the range of 0 - 20 Hz using equations 5 and 6, where subscripts *meas* and *corr* represent the measured and corrected forces and phase angles respectively.

$$F_{corr} = \frac{F_{meas}}{AR} \tag{5}$$

$$\phi_{corr} = \phi_{meas} + \theta \tag{6}$$

Once corrected, the measurements were converted back to real and imaginary components, then converted from the frequency domain back to the time domain. The corrected force measurements were then phase-averaged and converted to a time-dependent lift coefficient value, $c_l(t)$. For the periodic measurements, the phase-averaging process used a minimum of 100 deployment cycles. For transient measurements, 10 repeats were used.

The dynamic calibration results indicated that the entire system had a resonant frequency around 7.5Hz. The force measurement uncertainty near resonance was high, meaning that the aerodynamic forces could not be measured accurately. Using the methods of Moffat [28], the uncertainty in amplitude ratio and phase angle were assessed as ±10% and ±45° respectively at resonance, compared to a typical value of ±5% and ±2° across the rest of range of frequencies [1]. Measurements close to the resonant

frequency, between f = 6.5 Hz and 8 Hz (k = 0.51 to 0.59) were omitted due to the high measurement uncertainty. Table 1 summarizes the experimental parameters investigated using force measurements.

Table 1: Experimental parameters and uncertainties for force measurements.

Parameter	Value(s) Considered		Uncertainty
	Periodic	Transient	
h_{max}/c, mini-tab height	0.01, 0.015	0.01, 0.015	±0.00035
Re, Reynolds number	$6.6\text{x}10^5$	$6.6\text{x}10^5$	$\pm0.16\text{x}10^5$
α, Angle of Attack	0, 5, 8, 10 & 13°	0, 5, 8 & 10°	±0.25 °
k, actuation reduced frequency	0 to 0.79	-	±0.1 % f
τ_{deploy}, Deployment Period	-	1, 2, 3	±0.1 % τ_{deploy}

2.4 Particle Image Velocimetry Measurements

Cases of interest were selected from the periodic and transient force measurements for further analysis using Particle Image Velocimetry (PIV). A TSI-2D PIV system was used, which consisted of two eight Megapixel TSI PowerView CCD cameras (3,312 x 2,488 pixels) using Nikon 50mm Nikkor lenses, a double pulsed 200 mJ 15 Hz Nd:YAG Quantel Evergreen laser, a TSI LaserPulse synchronizer and a six jet TSI oil-droplet generator.

The two cameras were mounted on a traverse below the wind tunnel in a "tandem" configuration with a small overlap region (see Fig. 2(b)). They had the same, spanwise-normal plane of interest, located at z/b = 0.6, to avoid any reflections produced by pressure taps at the mid-span. The tandem setup allowed the full airfoil upper surface and wake to be captured in one set up, with an overall field of view of 0.8 x 0.3 m. In this paper, only the region of interest close to the airfoil trailing edge is presented to better show the subtle differences in the flow-field.

PIV measurement phase-locking, synchronization to a specific instance in the deployment cycle, used a pulse from the NI cRIO to the TSI laser synchronizer. For each case 500 image pairs per camera were concurrently acquired. TSI Insight 4G software determined the in-plane velocity vectors using a fast Fourier transform cross-correlation algorithm. An interrogation region of 32 x 32 pixels was chosen, producing a spatial resolution of 0.2%c. The vector fields from each camera were then averaged, producing a mean, phase-locked response. The overlap between the cameras (Fig. 1(b)) allowed each camera's vector fields to be combined. A weighted average was used within the overlap region with a bias towards the closer image center. The uncertainty in the averaged velocities was quantified as 1.25%U_∞ by combining the methods of Charonko & Vlachos [29] and Moffat [28]. The PIV measurement plane thickness was circa 2 mm, with an alignment error of ±1 mm. The experimental parameters used for the PIV measurements are summarized in Table 2.

Table 2: Experimental parameters and uncertainty for PIV measurements.

Parameter	Value(s) Considered		Uncertainty
	Periodic	Transient	
h_{max}/c, mini-tab height	0.015	0.015	±0.00035
Re, Reynolds number	6.6×10^5	6.6×10^5	$\pm 0.16 \times 10^5$
α, Angle of Attack	0 &10°	0°	±0.25°
k, Reduced Frequency	0, 0.20, 0.39 & 0.63	-	±0.1 % f
t/T, Normalized Phase Times	0, 0.25, 0.5, 0.75	-	+1%T
τ_{deploy}, Deployment Period	-	1	±0.1 %τ_{deploy}
τ_{deploy}/τ	-	0, 1, 2, 8	±1%τ_{deploy}

3. Results & Discussion

3.1 Description of Nomenclature

Figure 3 summarizes the nomenclature used to describe the lift response due to periodic (Fig. 3(a)) and transient (Fig. 3(b)) mini-tab actuation. The desired and measured mini-tab deployment are also indicated, with the mini-tab deployment shown in black and the lift response shown in red. These colors indicate their respective y-axis.

For periodic measurements (Fig 3(a)), the static change in lift, $\Delta c_{l,s}$ is defined as the difference between the time-averaged lift coefficient for the retracted mini-tab, $c_{l,h=0}$ and the time-averaged lift coefficient corresponding to the maximum mini-tab height, $c_{l,hmax}$. The mini-tab motion produces a time-dependent lift coefficient, $c_l(t)$. The phase-averaged time-dependent change in lift, $\Delta c_l(t)$ is defined as $c_l(t) - c_{l,h=0}$. Periodic mini-tab deployment produces a phase-averaged maximum, $c_{l,max}$ and minimum, $c_{l,min}$ lift coefficient. As such, the phase-averaged peak-to-peak change in lift is referred to as $c_{l,min} - c_{l,max}$.

For transient measurements (Fig 3(b)) the $\Delta c_{l,s}$ definition is the same. The desired deployment period is defined as τ_{deploy}. The time-dependent lift coefficient, $c_l(t)$ begins at a value corresponding to $h_{initial}$ and tends towards the value obtained for h_{final}, i.e., $c_{l,h=0}$ and $c_{l,hmax.}$

3.2 Static Measurements using a Deployable Mini-tab

Figure 4 presents the change in lift, $\Delta c_{l,s}$ for a statically deployed mini-tab for angles of attack: $0° \leq \alpha \leq 13°$ and heights: $0 \leq h/c \leq 0.015$. It is expected that $\Delta c_{l,s}$ is proportional to the square root of the normalized mini-tab height. This theory, developed by Liu & Montefort [30] and Woods [31] and shown in equation 7, has been shown to apply to wide range of airfoil profiles, for locations near the trailing edge and for the airfoil zero-lift angle [3].

$$\Delta c_{l,s} \propto (h/c)^{\frac{1}{2}} \tag{7}$$

This theoretical relationship is shown for $\alpha = 0°$ in Fig. 4. The results illustrate a disagreement between the theory and experimental results. At small mini-tab heights the gradient increases before reaching an inflexion point around $h/c = 0.0075$ and then decreasing as expected. This may be due to a number of factors, such as the mini-tab chord-wise location, $x_f/c = 0.85$ and the boundary layer reducing the mini-tab's influence. A cubic fit is presented as an improved approximation of the mini-tab's response and is presented as the dashed lines in Fig. 4. This will be used in section 3.3 to approximate the quasi-static response of the mini-tab.

Figure 4 also exhibits the expected trends with respect to α: change in lift, $\Delta c_{l,s}$ for a mini-tab height of $h/c = 0.015$ decreases from -0.17 to -0.04 as the angle of attack, α is increased from 0° to 13°. The reduction can be attributed to the flow separating ahead of the mini-tab location at high angles of attack, inhibiting the mini-tab's influence on the flow.

3.3 Periodic Mini-tab Deployment

Figure 5 presents $\Delta c_l(t)$ as a function of $h(t)/h_{max}$ for different actuation reduced frequencies, k and angles of attack, α for the maximum mini-tab deployment height: $h_{max}/c = 0.015$. Also displayed is the quasi-static response, indicated as $k \rightarrow 0$, representing a mini-tab deploying infinitesimally slowly such that it encounters no unsteady aerodynamic effects and therefore follows the cubic fit generated in section 3.2.

Figure 5(a) displays measurements for $\alpha = 0°$. For an actuation reduced frequency, $k = 0.16$ it is observed that $\Delta c_l(t)$ no longer follows the quasi-static response. Instead a clockwise hysteresis loop is formed, comparable to literature [10, 11, 14], indicative of a delay in aerodynamic response. In practice, this delay in response equates to a delay in aerodynamic load control. Understanding the magnitude of this effect, its cause and dependencies is therefore crucial. As k increases, the hysteresis loop pivots about its center, with the magnitude of $\Delta c_l(t)$ decreasing at $h(t)/h_{max} = 1$ and increasing at $h(t)/h_{max} = 0$. This results in the peak of $\Delta c_l(t)$ occurring later in the phase, such as for $k = 0.79$ where this occurs at $h(t)/h_{max} \approx 0.65$. Concurrently, it is observed that the peak-to-peak response, $c_{l,min} - c_{l,max}$ decreases from -0.17 for $k \rightarrow 0$ to -0.10 at $k = 0.79$.

Figure 6 presents the phase-averaged, time-dependent change in lift, $\Delta c_l(t)$ normalized by the steady-state value, $\Delta c_{l,s}$ as a function of the normalized time, t/T where T is the period of oscillation ($1/f$). By definition, the quasi-static ($k \rightarrow 0$) response displays a maximum value $\Delta c_l(t)/\Delta c_{l,s} = 1$ at $t/T = 0.5$, corresponding to the time where the mini-tab is at its maximum height. This response is not a perfect sine wave due to the non-linearity in $\Delta c_{l,s}$ with increasing mini-tab height, h/c, see Figure 4.

Figure 6(a) displays the results obtained at $\alpha = 0°$ and a maximum mini-tab height, $h_{max}/c = 0.015$. A reduction in the peak-to-peak amplitude is observed with increasing k, reducing to 0.78 at $k = 0.31$

and 0.6 at k = 0.79. At higher reduced frequencies the lift response becomes less sinusoidal resulting in a double peak for k = 0.63 and plateau for k = 0.79. As k increases the peak in $\Delta c_l(t)/\Delta c_{l,s}$ begins to shift to the right indicating increasing delay.

The effect of increasing the angle of attack, $5° \leq \alpha \leq 13°$ is observed in Figs. 5(b) to (e) and 6(b) to (e). In general, the trends displayed at $\alpha = 0°$ - an increase in phase angle with a decrease in lift reduction amplitude - are observed at the higher angles of attack, albeit with a decrease in $\Delta c_l(t)$. This decreasing $\Delta c_l(t)$ is best observed in Fig. 5(a) to (e) and is consistent with the decrease observed in Fig. 4 for the static change in lift, $\Delta c_{l,s}$. The reduction with increasing α and k means that the change in lift becomes extremely small, $(c_{l,min} - c_{l,max})$ = -0.016 for $\alpha = 13°$ and k = 0.79 so that the trends become barely visible. To draw comparison, it is instead necessary to consider the normalized curves, Fig. 6(b) to 6(e). Here it is possible to distinguish the decaying amplitude and increasing delay with increasing k and it is also possible to observe that the decay in amplitude increases with angle of attack. For example, compare k = 0.16 for $\alpha = 0°$ and $\alpha = 13°$.

The mini-tab frequency response was extracted from the phase-averaged measurements and is displayed in Figs. 7 and 8. The shaded area between $0.43 \leq k \leq 0.63$ represents resonance, where the uncertainty of the measurement was considered to be high. The normalized peak-to-peak change in lift, $(c_{l,min} - c_{l,max})/\Delta c_{l,s}$ and phase angle between mini-tab deployment and the lift response, φ are displayed as a function of k.

Figure 7(a) presents results obtained at $\alpha = 0°$. A decay in $(c_{l,min} - c_{l,max})/\Delta c_{l,s}$ can be observed with increasing k. The decay is independent of mini-tab height, with both heights, h_{max}/c = 0.01 (open square) and 0.015 (closed square) following the same trend. A first order fit of the data is provided and will be discussed in section 3.5. For h_{max}/c = 0.015, the lift response decreases to $(c_{l,min} - c_{l,max})/\Delta c_{l,s}$ = 0.6 at k = 0.79. Figure 7(a) includes Theordorsen's circulation function, $C(k)$ [12], which appears to have a good agreement with the results produced with an oscillating mini-tab. This result is surprising, given the derivation of Theodorsen's function, which is intended for pitching and plunging airfoils without any consideration for flow separation, as is produced by the mini-tab. The shapes of the first order fit and Theodorsen's function are different. The magnitude reduction with increasing frequency means the mini-tab has a limited effect at higher frequencies.

Figure. 7(a) includes other measurements, summarized in Table 3. In general, the trends observed in the present study agree with the wider literature. However, it is important to note that while the trends agree, there are large differences in $(c_{l,min} - c_{l,max})/\Delta c_{l,s}$. For example, around k = 0.2 a variation in $(c_{l,min} - c_{l,max})/\Delta c_{l,s}$ of almost 0.3 is noted. One possible hypothesis for the large disparities may be the testing conditions: the measurements span different Mach numbers, different airfoil profiles and different chordwise locations of the mini-tab (see Table 3).

Figures 7(b) to (e) show the effect of increasing angle of attack. This clearly shows that increasing α reduces the mini-tab's effectiveness at higher reduced frequencies. This is most noticeable for stall (α

= 13°, Fig. 7(e)), where a more rapid decrease in $(c_{l,min} - c_{l,max})/\Delta c_{l,s}$ is observed than for α = 0° (Fig. 7(a)). Thus, the similarity to Theodorsen's function is lost at higher angles of attack.

The lift response phase angle, φ is shown in Fig. 8 and is calculated from the lift response first harmonic, corresponding to the mini-tab actuation frequency. A more negative φ indicates a greater delay in lift response. The measurements for α = 0° (Fig. 8(a)) indicate a monotonic increase in the magnitude of φ with respect to k. The trend is independent of mini-tab maximum deployment with both heights, h_{max}/c = 0.01 and 0.015 in agreement. However, when compared to Theodorsen's circulation function there is little agreement, with much larger φ values obtained. This indicates that the agreement in Fig.7 may be purely coincidental. Characterization of this effect is of importance in the design of the load control actuation system. In mitigating the unsteady loads emanating from gusts and turbulence, it may be necessary to actuate ahead of the gust impacting the wing, in a "feed-forward" configuration. Sensors would be placed upstream, to account for the delay in aerodynamic response.

Figure 8(a) also compares φ values from literature to the present study. These measurements exhibit an extremely large range, with Lee & Kroo [7] in agreement with Theordorsen's function while others [9, 10] have a much larger phase delay. It appears that the mini-tab chordwise location, shown in Table 3, plays a large role in the phase angle, with greater φ values presented as the mini-tab is moved upstream of the trailing edge. However, as with $(c_{l,min} - c_{l,max})/\Delta c_{l,s}$, this hypothesis must be treated with caution due to the disparity in testing conditions. Comparing Figs. 8(a) to (e) it can be noted that φ increases with increasing α. There is greater scatter at the higher angles (see Fig. 8(e)) due to the reduced absolute amplitude of the lift signal increasing the relative measurement uncertainty. Using the methods described in [1], the uncertainty at 13° was up to ±20%.

Table 3: Details of literature studies used for comparison to the current study, α = 0°.

Literature Source	Test Conditions						Time Constant, κ	REF
	Airfoil Profile	Reynolds Number, *Re*	Mach Number, *Ma*	Chordwise Location, x_f/c	Maximum Amplitude, h_{max}/c	Surface		
Current Study	NACA0012	$Re = 6.6 \times 10^5$	$Ma = 0.06$	$x_f/c = 0.85$	0.015	Upper	1.06 to 1.13	N/A
Theodorsen, *C(k)*	N/A	Inviscid Theory	N/A	N/A	N/A	N/A	1.29	[12]
Clevenson & Tomassoni	NACA65-010	$Re = 2.7 \times 10^6$	$Ma = 0.2$	$x_f/c = 0.7$	0.021	Upper	1.04	[9]
Lee & Kroo	NACA0012	$Re = 1.5 \times 10^5$	N/A	$x_f/c = 1$ (Blunt TE)	0.01	Lower	1.77	[7]
Kinzel *et al*	VR-12	N/A	$Ma = 0.45$	$x_f/c = 0.9$	0.02	Lower	1.55	[10]
Kinzel *et al*	VR-12	N/A	$Ma = 0.60$	$x_f/c = 0.9$	0.02	Lower	1.12	[10]

Particle Image Velocimetry (PIV) measurements are used to investigate the mechanisms responsible for the delay in lift response and phase lag. Figures 9 and 10 display phase-locked velocity magnitude measurements for angles of attack, $\alpha = 0°$ and 10° for times $t/T = 0.0$, 0.25, 0.5 and 0.75 considering frequencies $k = 0$, 0.20, 0.39 and 0.63 with $h_{max}/c = 0.015$. The corresponding $\Delta c_l(t)/\Delta c_{l,s}$ measurements are shown above with red dashed lines indicating the four positions in the cycle.

The quasi-static response, $k \rightarrow 0$ at $\alpha = 0°$ is shown in the first row of Fig. 9. A normalized value of $t/T = 0.00$ corresponds to stowed mini-tab, while $t/T = 0.25$ and 0.75 correspond to $h/c = 0.0075$ and $t/T = 0.50$ corresponding to $h/c = 0.015$. In line with previous measurements [3], the separation region size increases with mini-tab height. The recirculation region is key to the mini-tab's efficacy, causing an effective decrease in the airfoil camber and therefore reduced lift.

The first column in Fig. 9 displays the flowfield for each k value when the mini-tab is fully stowed within the trailing edge section at $t/T = 0.00$. At this value the normalized lift response, $\Delta c_l(t)/\Delta c_{l,s}$ displays an increased value for $k = 0.63$ in comparison to $k \rightarrow 0$. Although the differences in the flowfield are small, it can be observed that the streamlines for $k = 0.63$ are angled upwards past the trailing edge. This indicates a decambering of the flow resulting in a decrease in lift.

At $t/T = 0.25$ (second column), the delay in lift response is more clearly observed. As k increases, the separated region behind the mini-tab decreases, indicating a reduction in effect. The clearest comparison is between $k \rightarrow 0$ and $k = 0.63$ where the separated region appears smaller for the periodically deploying mini-tab. At $t/T = 0.50$ the delay and reduction in efficacy is less clear. The delay is less clear due to the plateau in the sine profile motion making changes in height, and thus flowfield, more gradual. Measurements presented elsewhere [1] have shown that this reduction in effectiveness is due to delay in the upstream propagation of the effect. This is despite the relatively large differences in $\Delta c_l(t)/\Delta c_{l,s}$ present at $t/T = 0.50$. At a normalized time, $t/T = 0.75$ the effect of reduced frequency is once again easily observable. At this position, the mini-tab is retracting and thus a lag in response is indicated by an increase in the separation region's size. This is observable in Fig. 9, where moving from $k = 0.20$ to 0.63 produces a larger separated region and a greater lift reduction when compared to $k \rightarrow 0$.

The flow field measurements indicate that the delay and reduction in efficacy for a periodically deploying mini-tab is related to the growth and size of the mini-tab separation region and its ability to alter the wake angle. As with static deployment, a smaller separation region yields less influence on the flow, resulting in a smaller change in lift. This hypothesis agrees with the Schlieren measurements of Clevenson & Tomassoni [9], who obtained a similar trend in $(c_{l,min} - c_{l,max})/\Delta c_{l,s}$ (see Fig. 7(a)). The mini-tab was shown to produce a region of separated flow which was larger during the inward (t/T = 0.5 to 1) phase of deployment than in the outward, deploying phase. However, the computations of Kinzel *et al* [10] produced a coherent vortical structure behind the mini-tab which was larger on the outward than during the inward deployment phase. In the present study, the coherent vortex structure and adverse lift response were not observed. Instead, the separated shear layer produced by the mini-tab suggests that the vortical structure was shed into the wake before it could coherently develop.

The effects of increasing the angle of attack, α on periodic mini-tab deployment can be observed by comparing Fig. 9 ($\alpha = 0°$) with Fig. 10 ($\alpha = 10°$). For $\alpha = 10°$ the quasi-static ($k \rightarrow 0$) response at t/T = 0.00 indicates that the flow separates ahead of the trailing edge, consistent with trailing edge stall. The quasi-static response illustrates that the mini-tab is submerged in the separated flow, causing a reduction in the mini-tab's efficacy even in static conditions, see Figure 4. In general, the trends noted at $\alpha = 0°$ also apply at this higher angles of attack but with reduced amplitude, i.e., the flow separation decreasing in size on the outward portion of deployment (t/T = 0.25) and increasing in size on the inward portion (t/T = 0.75) when k is increased. However, as the lift response indicates, the presence of the baseline flow separation in the vicinity of the mini-tab reduces its effect with increasing k.

3.4 Transient Mini-tab Deployment

The mini-tab transient lift response is shown in Fig. 11, where the normalized time-dependent change in lift coefficient, $\Delta c_l(t)/\Delta c_{l,s}$ is presented as a function of non-dimensional time, τ for the maximum mini-tab height, h_{max}/c = 0.015 at $\alpha = 0°$. Also presented are the desired mini-tab deployment profiles, $h(t)/h_{max}$ (open square symbols) and measured deployment profile $h(t)_{meas}/h_{max}$ (solid triangle symbols), as well as a first order fit to the measured lift. In certain cases, the measured mini-tab deployment lags the desired profile due to limited acceleration combined with the desire for stable, damped, motion. For a desired τ_{deploy} = 1, measured value of τ_{deploy} = 1.24 and 1.02 for outward and inward deployment directions respectively.

Figure 11(a) presents results for an outward motion (the mini-tab moves from h/c = 0 to h_{max}/c = 0.015) for a deployment period, τ_{deploy} = 1. The mini-tab's aerodynamic response lags the motion profile and only attains the final value at $\tau \approx 6$, significantly after the mini-tab motion is completed. Increasing the deployment period to τ_{deploy} = 2 and 3 produces a similar aerodynamic lag, as shown in Figs. 11(b) and (c), attaining the final, static value between τ = 6 and 7. Inward motion (Figs. 11(d) to (f)) reaches the final static value between τ = 4 and 5: faster than outward motion.

Figure 12 shows measurements obtained for $0° \leq \alpha \leq 10°$: the static change in lift was too small at α = 13° to accurately evaluate the transient aerodynamic response. Figure 12(a) compares the transient response at different α for the same deployment period, τ_{deploy} = 1 and maximum height, h_{max}/c = 0.015. The lag in aerodynamic response increases with α. For example, the lift response at $\alpha = 0°$ reaches the static maximum value within 4-5 non-dimensional time units (τ); $\alpha = 5°$ is almost identical whereas α = 8° and 10° clearly lag and do not reach the maximum value within τ = 10. This is consistent with the periodic deployment measurements, where a greater aerodynamic lag was measured as an increase in phase angle, φ. Comparing Figs. 12(a) and (b) it is clear that this trend is also consistent for inward deployment.

Overall, the force measurements indicate the presence of a lag in lift response for transient mini-tab deployment. To investigate the cause of the lag, flow field measurements are shown in Figs 13 and 14

for $\alpha = 0°$ considering both outward and inward motions of period, $\tau_{deploy} = 1$. Velocity magnitude in the flow fields are shown for the initial condition ($\tau/\tau_{deploy} = 0$), when the final height is attained ($\tau/\tau_{deploy} = 1$), during the lag ($\tau/\tau_{deploy} = 2$) and once the flow field has effectively reached steady-state ($\tau/\tau_{deploy} = 8$). Due to differences between the desired and measured mini-tab deployment profiles, PIV measurements were fixed relative to the measured mini-tab deployment, which had periods of $\tau_{deploy} = 1.24$ and 1.02 for outward and inward deployment directions respectively. The transient force measurements are presented in Figs. 13 and 14 above the PIV measurements to allow direct comparison.

Fig. 13(a) presents the flowfield before mini-tab deployment with no flow separation present. At $\tau/\tau_{deploy} = 1$ (Fig. 13(b)), the flow behind the mini-tab has begun to separate, but does not resemble that for static deployment. The streamlines beyond the airfoil trailing edge remain undeflected, indicating that the Kutta condition remains largely unchanged. In comparison, the flowfield at $\tau/\tau_{deploy} = 2$ (Fig. 13(c)) more closely resembles that obtained during static deployment. However, the lift response of $\Delta c_l(t)/\Delta c_{l,s} = 0.55$ indicates a significant lag. Examining the flowfield carefully, some unsteadiness in the downstream flow of the separated region suggests continued flow development. At $\tau/\tau_{deploy} = 8$ (Fig. 13(d)), the flowfield has stabilized, with deflected streamlines indicating the change in lift. This supports the force measurements which indicate that the static, final value has been obtained.

Figure 14 presents the flowfield for inward motion ($h(t)/h_{max}$ decreasing from 1 to 0). At $\tau/\tau_{deploy} = 0$ (Fig. 14(a)), the flowfield displays the initial condition: flow separation behind the mini-tab with a deflected wake, indicative of lift reduction. Figure 14(b) presents the flowfield at the end of the deployment phase ($\tau/\tau_{deploy} = 1$) at which the lift response has reduced to $\Delta c_l(t)/\Delta c_{l,s} = 0.8$. While the flow separation has reduced in size, the wake remains deflected. Between Figs. 14(b) and (d) a gradual reduction in the deflection in the wake can be observed, culminating in the flowfield returning to that expected for the baseline flow at $\tau/\tau_{deploy} = 8$ in agreement with the lift coefficient measurements.

In summary, the development of the transient lift response is intrinsically linked to the development of the separation region behind the mini-tab and the resulting wake deflection. The development of the flow is faster for inward deployment than outward deployment resulting in a faster lift response. The vortical structure and adverse effect on the observed in the computational studies of Chow & Van Dam [15], Vieira & Maughmer and Coder *et al.* [13, 16] is not observed in the present study. The results produced compare favorably to the experimental measurements of Bach [17], where no adverse lift response was observed across a range of deployment periods. In both computational and experimental studies a lag in the lift response is observed.

3.5 Modelling of Aerodynamic Response

The lift response of the periodic and transient motion both show behavior typical of a first order system. A fit is applied in the frequency and time domains for periodic and transient mini-tab deployment respectively in order to generate a characteristic non-dimensional time constant, κ which

defines the response of the aerodynamic system. This approximation is especially relevant to the design of the aerodynamic load controller, where knowledge of the expected response due to mini-tab deployment is needed and where the expected delay in response needs to be accounted for.

For periodic motions the frequency response can be approximated via a least squares curve fit of the data displayed in Fig. 7 using equation 8. This is the sinusoidal response of a 1st order system [32], expressed non-dimensionally. The non-dimensional time constant, κ defines the decay of $(c_{l,min} - c_{l,max})/\Delta c_{l,s}$ with increasing actuation reduced frequency, k.

$$\frac{c_{l,min} - c_{l,max}}{\Delta c_{l,s}} = \frac{1}{\sqrt{(2\kappa k)^2 + 1}} \tag{8}$$

Figure 15 presents the calculated κ values for periodic motion (grey square symbols) for $0° \leq \alpha \leq 10°$ and both maximum deployment heights: $h_{max}/c = 0.01$ (Fig. 15(a)) and 0.015 (Fig. 15(b)). At $\alpha = 0°$, the two heights have similar κ values: $\kappa = 1.06$ and 1.13 for $h_{max}/c = 0.01$ and 0.015 respectively. As α increases, the value of κ increases to 2.1 and 2.17 at $\alpha = 10°$, illustrating the expected increase in aerodynamic lag with increasing α. A greater κ value indicates that the system takes longer to reach a steady state value when a step input is applied. In a periodic system, this would mean that the changes in circulation initiated by the periodically deploying mini-tab have a decreasing effect on lift. In addition, time constant values can also be extracted from the literature measurements presented in Fig. 7(a). These values are presented in Table 3, along with the value generated for Theodorsen's function, $\kappa = 1.29$, using the least squares method between $k = 0$ and 1. In general, it can be noted that the present experimental study agrees well with the literature, with similar κ values.

For transient motion, an estimated time constant can be completed in the time domain. The model is chosen as the response of a first order system to a combination ramp-step input [32], where the step has a defined period (τ_{deploy}). Examples of this fit are shown in Fig. 11. The input profile is defined in equation 9.

$$I(\tau) = \frac{1}{\tau_{deploy}}\left[\tau \times u(\tau) - (\tau - \tau_{deploy}) \times u(\tau - \tau_{deploy})\right] \qquad where \qquad I(\tau) = \frac{h(\tau)}{h_{max}} \tag{9}$$

In equation 9, $u(\tau)$ represents the Heaviside step function [33]. The overall function, $I(\tau)$ is the superposition of two ramp functions: one positive starting at $\tau = 0$ and of gradient $1/\tau_{deploy}$ such that its value at $\tau_{deploy} = 1$ is unity. The second part of the equation applies a negative ramp function at $\tau = \tau_{deploy}$ to cancel out the positive ramp function and maintain a value of one. As the response of a first order system is known for both a ramp and a step function, the overall aerodynamic response can be approximated as:

$$\frac{\Delta c_l(\tau)}{\Delta c_{l,s}} = \frac{1}{\tau_{deploy}}\left[\left(\tau - \kappa\left(1 - e^{-\frac{\tau}{\kappa}}\right)\right) \times u(\tau) - \left((\tau - \tau_{deploy}) - \kappa\left(1 - e^{-\frac{\tau - \tau_{deploy}}{\kappa}}\right)\right) \times u(\tau - \tau_{deploy})\right] \tag{10}$$

The non-dimensional time constant, κ values generated using this function are plotted in Fig. 15 for inward (closed circles) and outward (open circles) deployment directions with $\tau_{deploy} = 1$. It is noted that κ is smaller for the inward direction than the outward direction, for example at $\alpha = 0°$ where respective values of 1.44 and 1.91 are obtained for $h_{max}/c = 0.01$. This is indicative of the smaller lag for inward deployment, as noted from the force measurements. Comparing κ for transient and periodic deployment in Figs. 15(a) and (b) indicates slightly lower values for periodic measurements than transient. Note that there is a larger uncertainty in the estimates for the periodic motion. However, both deployment profiles exhibit similar trends: κ increases as the angle of attack increases.

Additionally, the same analysis was performed using the results of Darabi & Wygnanski [34, 35], which considered a deflected flap and a periodically driven flow control device to initiate and control separation. In general, the flow in these experiments took longer to reach a steady-state, final value: typically, between 20 and 40 convective timescales. This is reflected in a larger time constant value, which was between 5 and 12. While the time constant generated was higher, the order of κ is similar to the experiments conducted in this study. The larger time constant can be attributed to the actuation being placed further upstream, resulting in a larger delay in aerodynamic response.

Chow & Van Dam [15] compared the aerodynamic response of a deploying mini-tab to Wagner's function, which represents the response to a step change in circulation, reaching 50% of the final value instantaneously. Wagner's function is represented by the summation of two exponential functions as shown in equation 11 after Jones [36], meaning that a first order approximation is insufficient.

$$W(\tau) = 1 - 0.165e^{-0.0455(2\tau)} - 0.335e^{-0.3(2\tau)} \quad (11)$$

Figure 16 compares the present study to Wagner's function. The half sine-step input profile split into a series of step functions, and the overall aerodynamic response is represented as a convolution of these individual steps with Wagner's function. It is notable that the initial lift response produced by the Wagner convolution is much faster than the actual response. As with Theodorsen's function, Wagner's function considers inviscid, attached flows. In the present study, the initialization, growth and stabilization of the separation region behind the mini-tab produces an aerodynamic effect which causes the longer lag in lift response. It is therefore not applicable or representative of the behavior. On the other hand, a simple first-order system can reproduce the measured lift, as shown in Figure 16.

4 Conclusions

The unsteady aerodynamic response of a dynamically deploying mini-tab was assessed using experimental wind tunnel measurements, necessary for effective load control system design. This study indicates significant unsteady aerodynamic effects of both periodic and transient mini-tab deployments.

For periodic (sinusoidal) deployment, the amplitude of lift reduction decreased as the actuation reduced frequency increased, reducing by 45% at k = 0.79 for $\alpha = 0°$, comparable to Theodorsen's circulation function. However, the amplitude decay is accompanied by a significant phase lag between actuation and lift response, lagging by φ = 101° at k = 0.79, which is much larger than that predicted by Theodorsen's function. Increasing the airfoil angle of attack produces a further reduction in effectiveness. Transient deployment displayed a sensitivity to the mini-tab deployment direction, with a larger delay in response for inward than outward deployment. Flowfield measurements indicate that the delay in response is related to the delay in development of the flow separation behind the mini-tab. A simple model was constructed for the mini-tab's aerodynamic response, approximating it as the response of a first order system. This defines a single dimensionless time constant, κ to be used in the design of a load control system. Increasing the angle of attack accelerates the decay in amplitude for periodic deployment, coupled with a larger phase lag. This results in an increase in the time constant, from κ = 1.1 to 4 between α = 0° and 13°, with similar effects observed for transient mini-tab deployment. These findings show the capability of the mini-tab to produce unsteady changes in lift, albeit with reduced amplitude and phase lag, at the higher reduced frequencies typical of the gusts and turbulence encountered by civil transport aircraft, and that this behavior can be reasonably modelled as a simple first order system.

Acknowledgments

The authors would like to thank Airbus UK for the financial support supplied to this project. A University Research Studentship from the University of Bath supported the lead author's work. The project was also assisted by EPSRC strategic equipment grant (EP/K040391/1 & EP/M000559/1) and EPSRC project (EP/M022307/1).

References

1. Heathcote, D. J., "Aerodynamic Loads Alleviation using Mini-tabs", PhD Thesis, Unversity of Bath, Bath, United Kingdom, 2017.

2. Heathcote, D. J., Gursul, I., and Cleaver, D. J., "An Experimental Study of Mini-Tabs for Aerodynamic Load Control," *54th AIAA Aerospace Sciences Meeting*, AIAA-2016-0325, San Diego, CA, USA, AIAA, 2016.

3. Heathcote, D. J., Gursul, I., and Cleaver, D. J., "Aerodynamic Load Alleviation Using Mini-tabs," *Journal of Aircraft*, Vol. 55, No. 5, 2018, pp. 2068-2077.

4. Palacios, J., Kinzel, M., Overmeyer, A., and Szefi, J., "Active Gurney Flaps: Their Application in a Rotor Blade Centrifugal Field," *Journal of Aircraft*, Vol. 51, No. 2, 2014, pp. 473-489.

5. Matalanis, C. G., Wake, B. E., Opoku, D., Min, B.-Y., Yeshala, N., and Sankar, L., "Aerodynamic Evaluation of Miniature Trailing-Edge Effectors for Active Rotor Control," *Journal of Aircraft*, Vol. 48, No. 3, 2011, pp. 995-1004.

6. Bieniawski, S., and Kroo, I., "Flutter Suppression Using Micro-Trailing Edge Effectors," *44th AIAA/ASME/ASCE/AHS/ASC Structures, Structural Dynamics, and Materials Conference*, AIAA-2003-1941, Norfolk, VA, USA, AIAA, 2003.

7. Lee, H.-T., and Kroo, I., "Computational Investigation of Airfoils with Miniature Trailing Edge Control Surfaces," *42nd AIAA Aerospace Sciences Meeting and Exhibit,* AIAA-2004-1051, Reno, NV, USA, AIAA, 2004.

8. Wilson, D. G., Berg, D. E., Lobitz, D. W., and Zayas, J. R., "Optimized Active Aerodynamic Blade Control for Load Alleviation on Large Wind Turbines," *AWEA WINDPOWER 2008 Conference & Exhibition,* , Houston, TX, 2008.

9. Clevenson, S. A., and Tomassoni, J. E., "Experimental Investigation of the Oscillating Forces and Moments on a Two-dimensional Wing Equipped with an Oscillating Circular-arc Spoiler." NACA Technical Note 3949, 1954.

10. Kinzel, M. P., Maughmer, M. D., and N. Duque, E. P., "Numerical Investigation on the Aerodynamics of Oscillating Airfoils with Deployable Gurney Flaps," *AIAA Journal*, Vol. 48, No. 7, 2010, pp. 1457-1469.

11. Tang, D., and Dowell, E. H., "Aerodynamic Loading for an Airfoil with an Oscillating Gurney Flap," *Journal of Aircraft*, Vol. 44, No. 4, 2007, pp. 1245-1257.

12. Theodorsen, T., "General Theory of Aerodynamic Instability and The Mechanism Of Flutter." NACA Technical Note No. 496, 1935.

13. Vieira, B. A. O., and Maughmer, M. D., "Unsteady Aerodynamic Model for Deployable Gurney Flaps Based on Indicial Concepts," *Journal of Aircraft*, 2016, pp. 1-13.

14. Liu, L., Padthe, A. K., and Friedmann, P. P., "Computational Study of Microflaps with Application to Vibration Reduction in Helicopter Rotors," *AIAA Journal*, Vol. 49, No. 7, 2011, pp. 1450-1465.

15. Chow, R., and van Dam, C. P., "Unsteady Computational Investigations of Deploying Load Control Microtabs," *Journal of Aircraft*, Vol. 43, No. 5, 2006, pp. 1458-1469.

16. Coder, J. G., Maughmer, M. D., and Martin, P., B, "CFD Investigation of Unsteady Rotorcraft Airfoil Aerodynamics: MiTEs and Dynamic Stall," *49th AIAA Aerospace Sciences Meeting including the New Horizons Forum and Aerospace Exposition,* AIAA-2011-1125, Orlando, FL, USA, AIAA, 2011.

17. Bach, A. B., "Gurney Flaps and Micro-Tabs for Load Control on Wind Turbines", PhD Thesis, Technische Unversitat Berlin, Berlin, 2016.

18. Bach, A., B, Berg, R., Pechlivanoglou, G., Nayeri, C., and Paschereit, C., O., "Experimental Investigation of the Aerodynamic Lift Response of an Active Finite Gurney Flap," *53rd AIAA Aerospace Sciences Meeting*, AIAA-2015-1270, Orlando, FL, USA, AIAA, 2015.

19. Nikoueeyan, P., Strike, J., A. , Magstadt, A., S. , Hind, M., and Naughton, J., W. , "Aerodynamic Response of a Wind Turbine Airfoil to Gurney Flap Deployment," *33rd Wind Energy Symposium*, AIAA-2015-0995, Orlando, FL, USA, AIAA, 2015.

20. Barlow, J., Rae, W., and Pope, A., *Low-Speed Wind Tunnel Testing*, 3rd Edition, John Wiley & Sons, New York, 1999. pp. 306–311.

21. Pankhurst, R. C., and Holder, D. W., *Wind-Tunnel Technique: An Account of Experimental Methods in Low-and High-Speed Wind Tunnels*, 1st Edition, Pitman, London, 1952. pp. 320–349, 462–464.

22. Jacobs, E. N., and Sherman, A., "Airfoil Section Characteristics as Affected by Variations of the Reynolds Number." NACA Report No. 586, 1937.

23. Al-Battal, N. H., Cleaver, D. J., and Gursul, I., "Lift Reduction by Counter Flowing Wall Jets," *Aerospace Science and Technology*, Vol. 78, 2018, pp. 682-695.

24. Li, Y., Wang, J., and Zhang, P., "Influences of Mounting Angles and Locations on the Effects of Gurney Flaps," *Journal of Aircraft*, Vol. 40, No. 3, 2003, pp. 494-498.

25. Tsai, K.-C., Pan, C.-T., Cooperman, A. M., Johnson, S. J., and van Dam, C., "An Innovative Design of a Microtab Deployment Mechanism for Active Aerodynamic Load Control," *Energies*, Vol. 8, No. 6, 2015, pp. 5885-5897.

26. Chiereghin, N., Cleaver, D. J., and Gursul, I., "Unsteady Lift and Moment of a Periodically Plunging Airfoil," *AIAA Journal*, Vol. 57, No. 1, 2018, pp. 208-222.

27. Kumme, R., "Dynamic Force Measurement in Practical Applications," *Proceedings of XVI IMEKO World Congress*, Vienna, IMEKO, 2000.

28. Moffat, R. J., "Describing the Uncertainties in Experimental Results," *Experimental Thermal and Fluid Science*, Vol. 1, No. 1, 1988, pp. 3-17.

29. Charonko, J. J., and Vlachos, P. P., "Estimation of Uncertainty Bounds For Individual Particle Image Velocimetry Measurements From Cross-Correlation Peak Ratio," *Measurement Science and Technology*, Vol. 24, No. 6, 2013, pp. 065301.

30. Liu, T., and Montefort, J., "Thin-Airfoil Theoretical Interpretation for Gurney Flap Lift Enhancement," *Journal of Aircraft*, Vol. 44, No. 2, 2007, pp. 667-671.

31. Woods, L. C., *The theory of subsonic plane flow*, Cambridge University Press, London, 1961. pp. 447-449.

32. Doebelin, E., *Control Systems Engineering*, CRC Press, 1998.

33. Bracewell, R., "Heaviside's Unit Step Function", *The Fourier Transform and Its Applications*, 3rd Edition, McGraw-Hill, 2000. pp. 61-65.

34. Darabi, A., and Wygnanski, I., "Active management of naturally separated flow over a solid surface. Part 1. The forced reattachment process," *Journal of Fluid Mechanics*, Vol. 510, 2004, pp. 105-129.

35. Darabi, A., and Wygnanski, I., "Active management of naturally separated flow over a solid surface. Part 2. The separation process," *Journal of Fluid Mechanics*, Vol. 510, 2004, pp. 131-144.

36. Jones, R. T., "The Unsteady Lift of a Wing of Finite Aspect Ratio." NACA Technical Report No. 681, 1940.

Figures

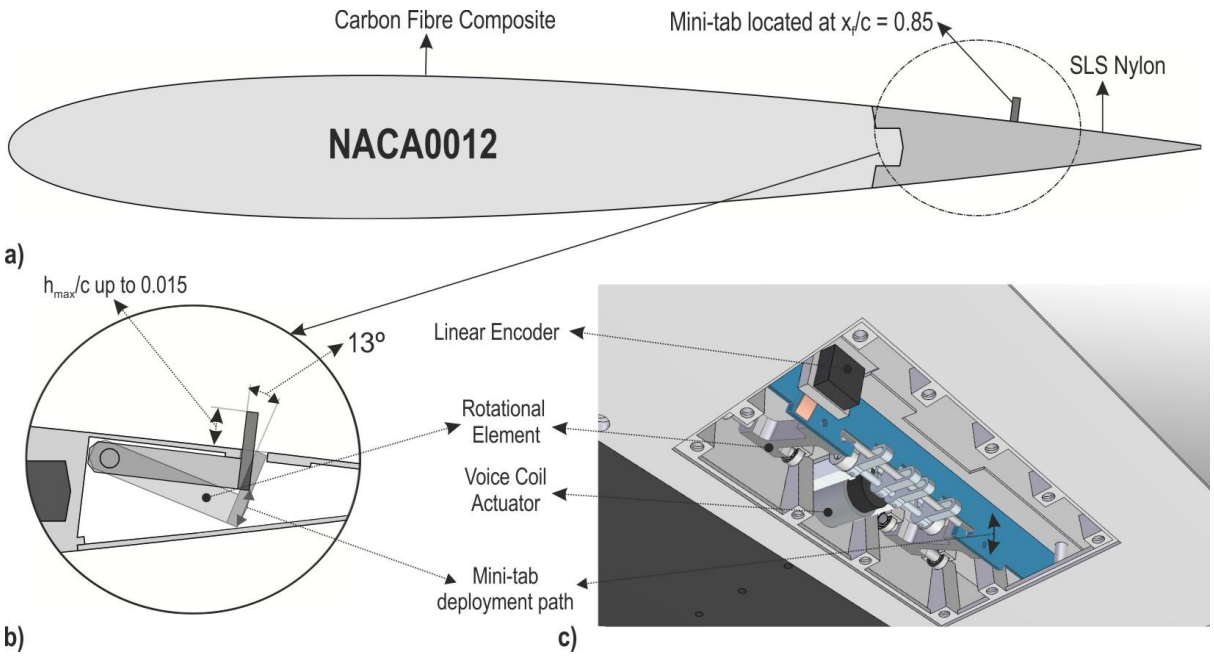

Figure 1: (a) NACA0012 including mini-tab location, (b) mini-tab motion (c) the trailing edge section interior.

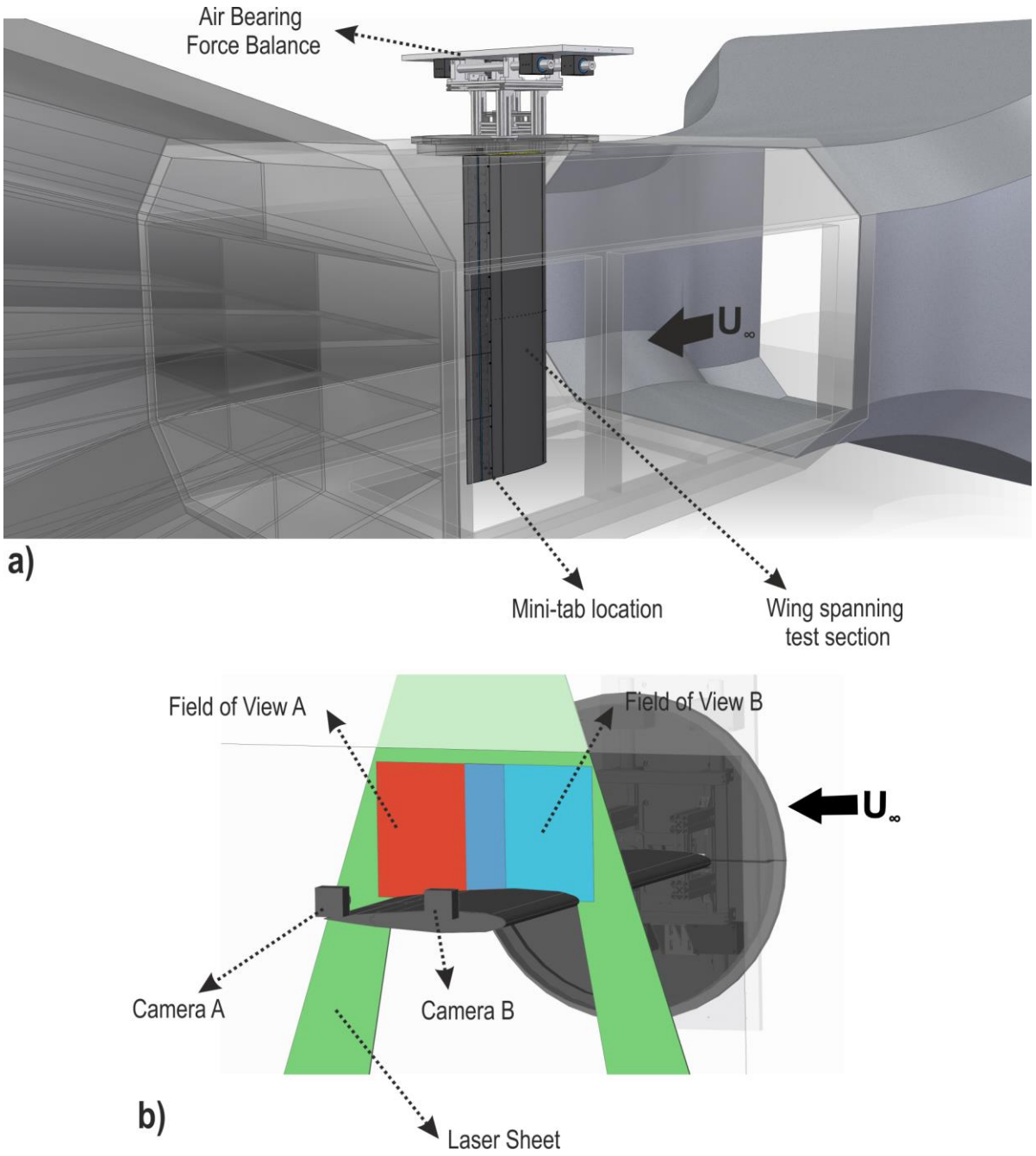

Figure 2: (a) Experimental set up, (b) PIV set up with tandem cameras.

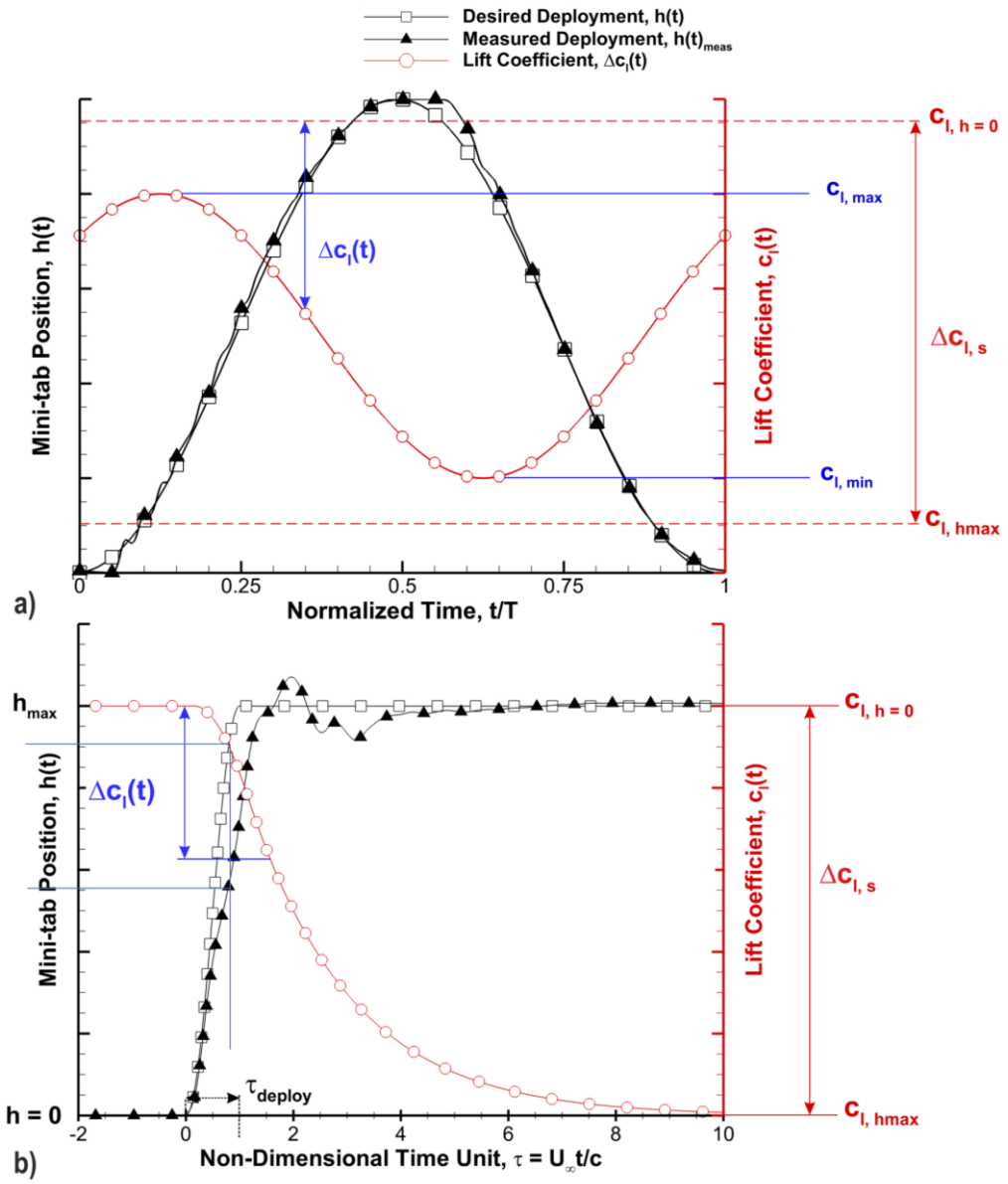

Figure 3: Description of nomenclature for (a) periodic force measurements and (b) transient force measurements.

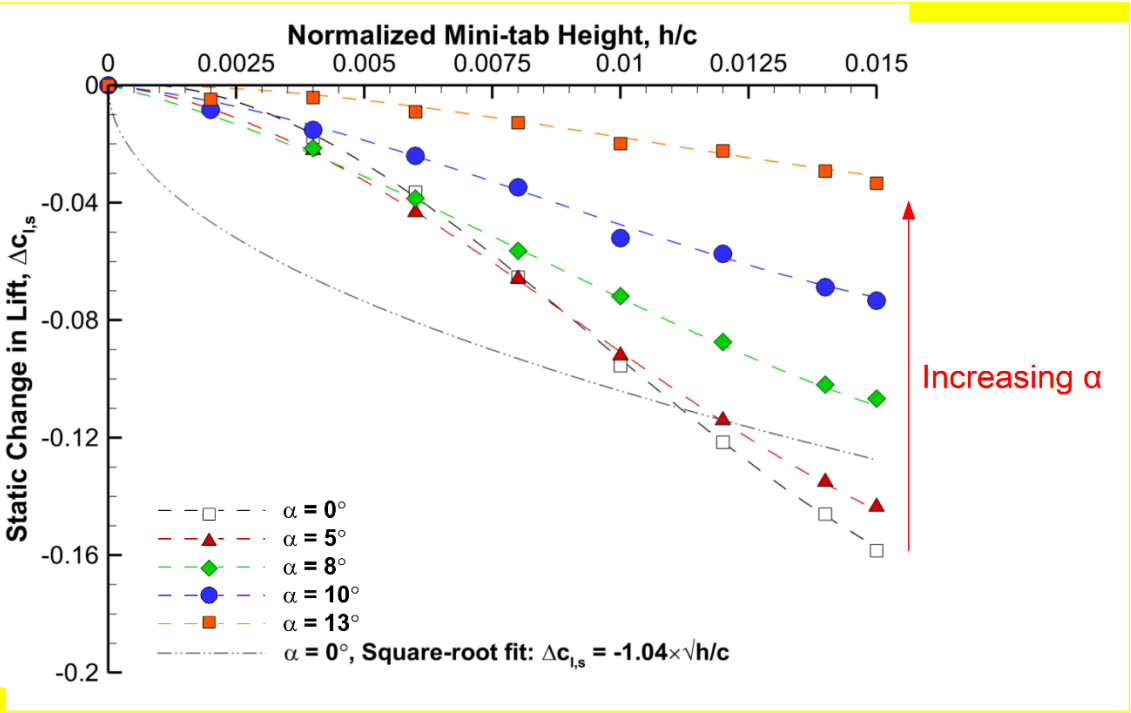

Figure 4: Static change in lift coefficient vs. normalized mini-tab height for α = 0° to 13°, including best fit 3rd order polynomial and square root relationship

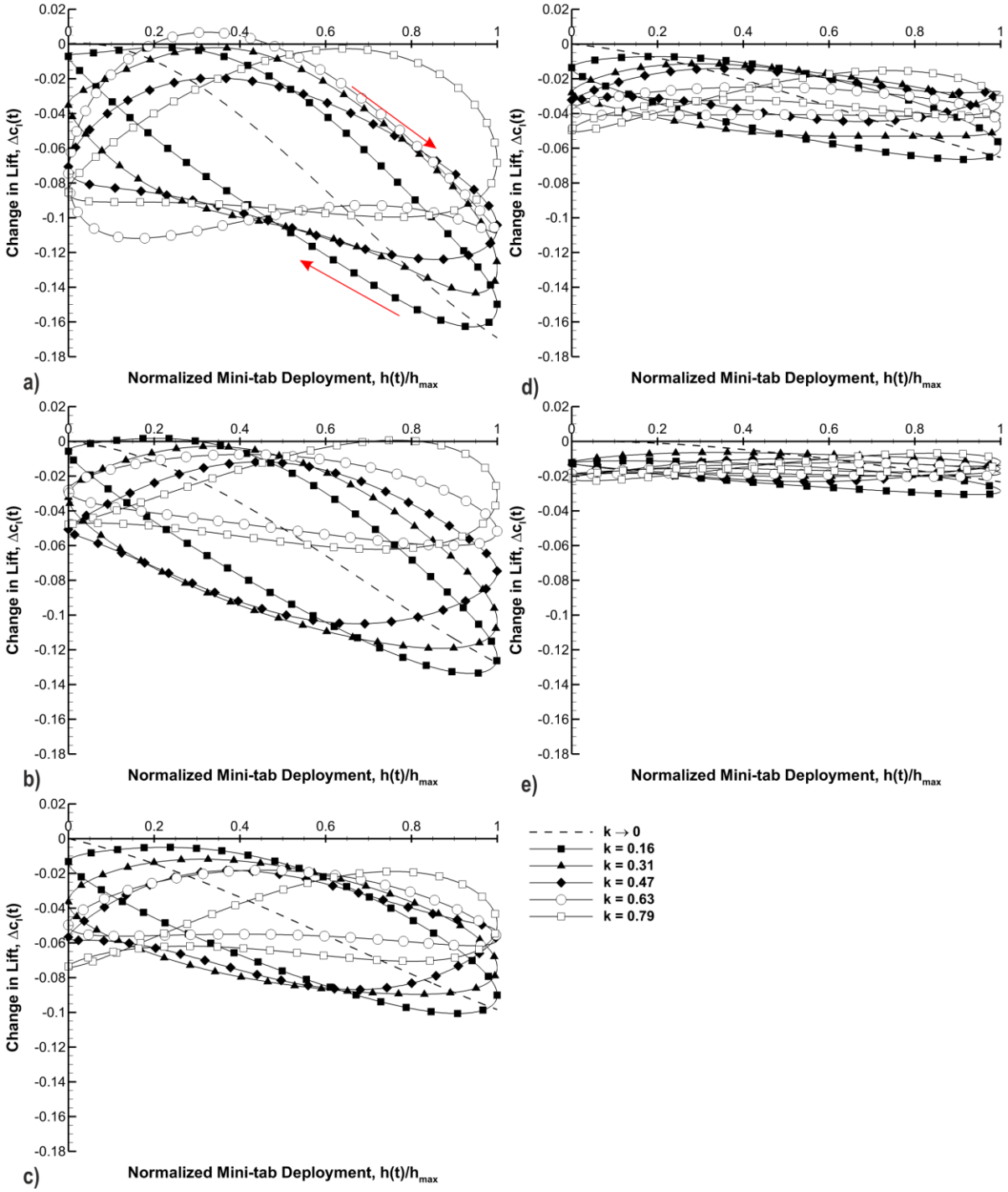

Figure 5: Periodic motion hysteresis loops for $h_{max}/c = 0.015$ and angles of attack: (a) $\alpha = 0°$, (b) $\alpha = 5°$, (c) $\alpha = 8°$, (d) $\alpha = 10°$ and (e) $\alpha = 13°$.

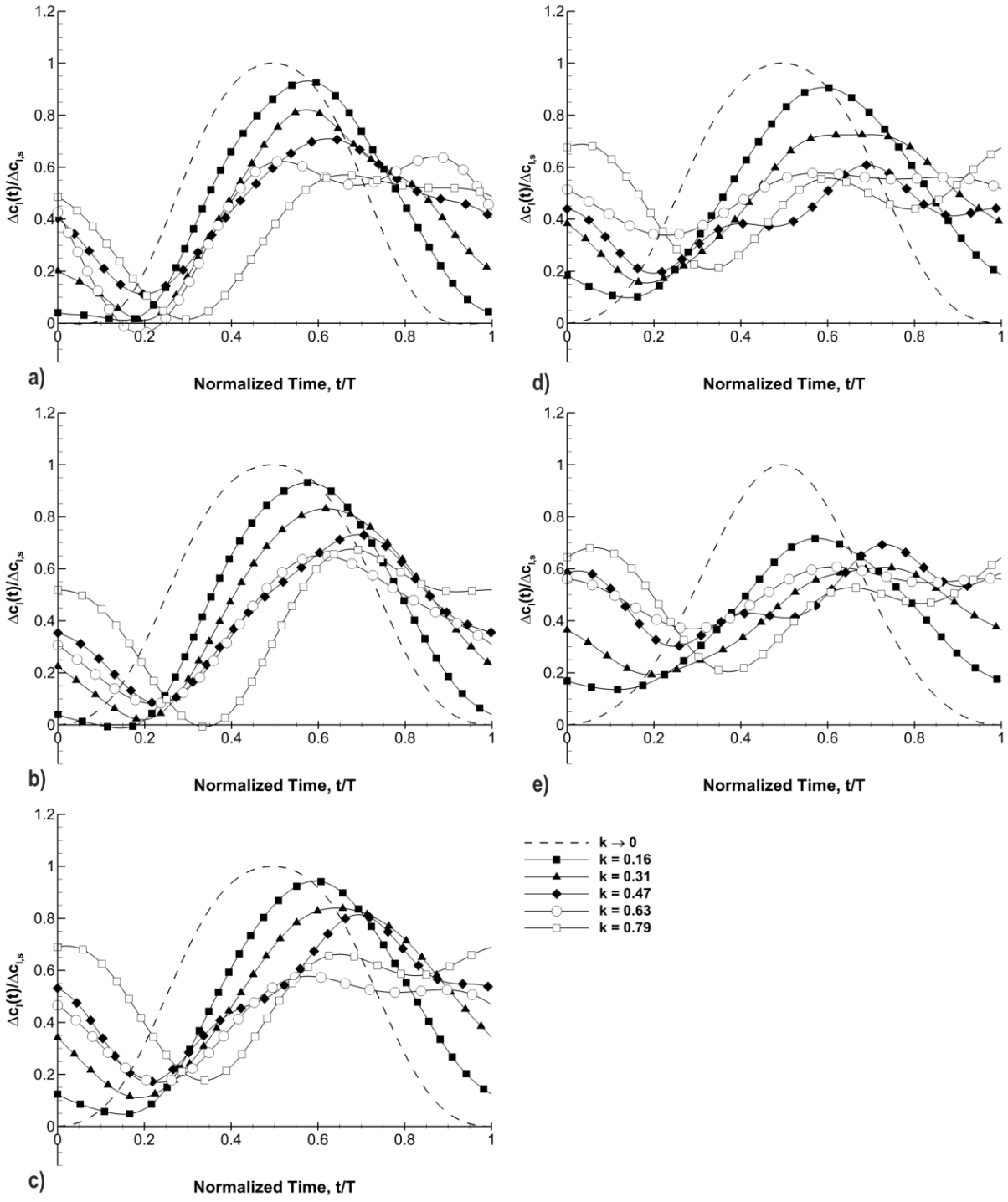

Figure 6: Periodic motion time variant lift response for $h_{max}/c = 0.015$ and angles of attack: (a) $\alpha = 0°$, (b) $\alpha = 5°$, (c) $\alpha = 8°$, (d) $\alpha = 10°$ and (e) $\alpha = 13°$.

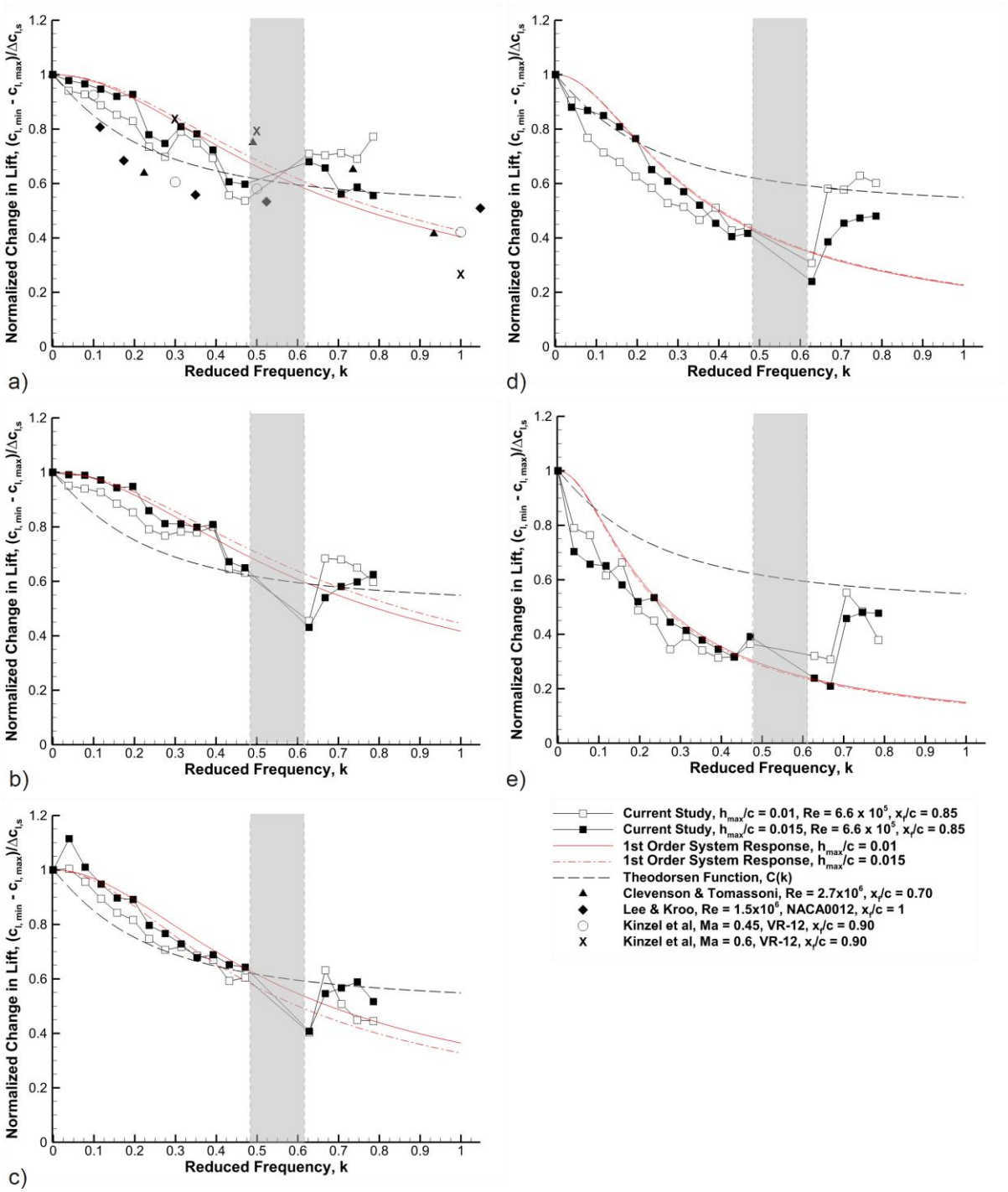

Figure 7: Periodic motion amplitude decay for h_{max}/c = 0.01 and 0.015 at (a) α = 0°, (b) α = 5°, (c) α = 8°, (d) α = 10° and (e) α = 13°.

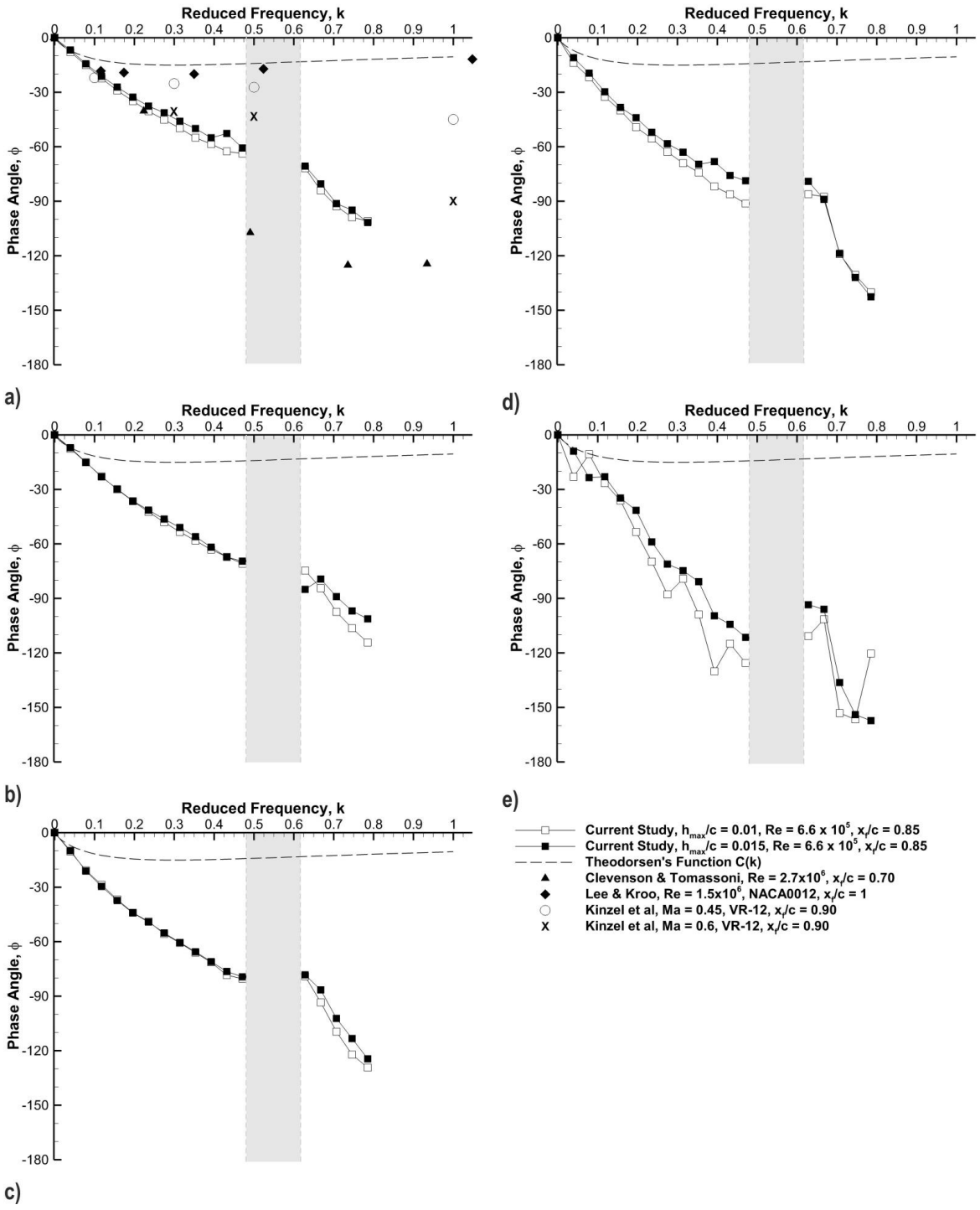

Figure 8: Periodic motion phase angle for h_{max}/c = 0.01 and 0.015 at (a) α = 0°, (b) α = 5°, (c) α = 8°, (d) α = 10° and (e) α = 13°.

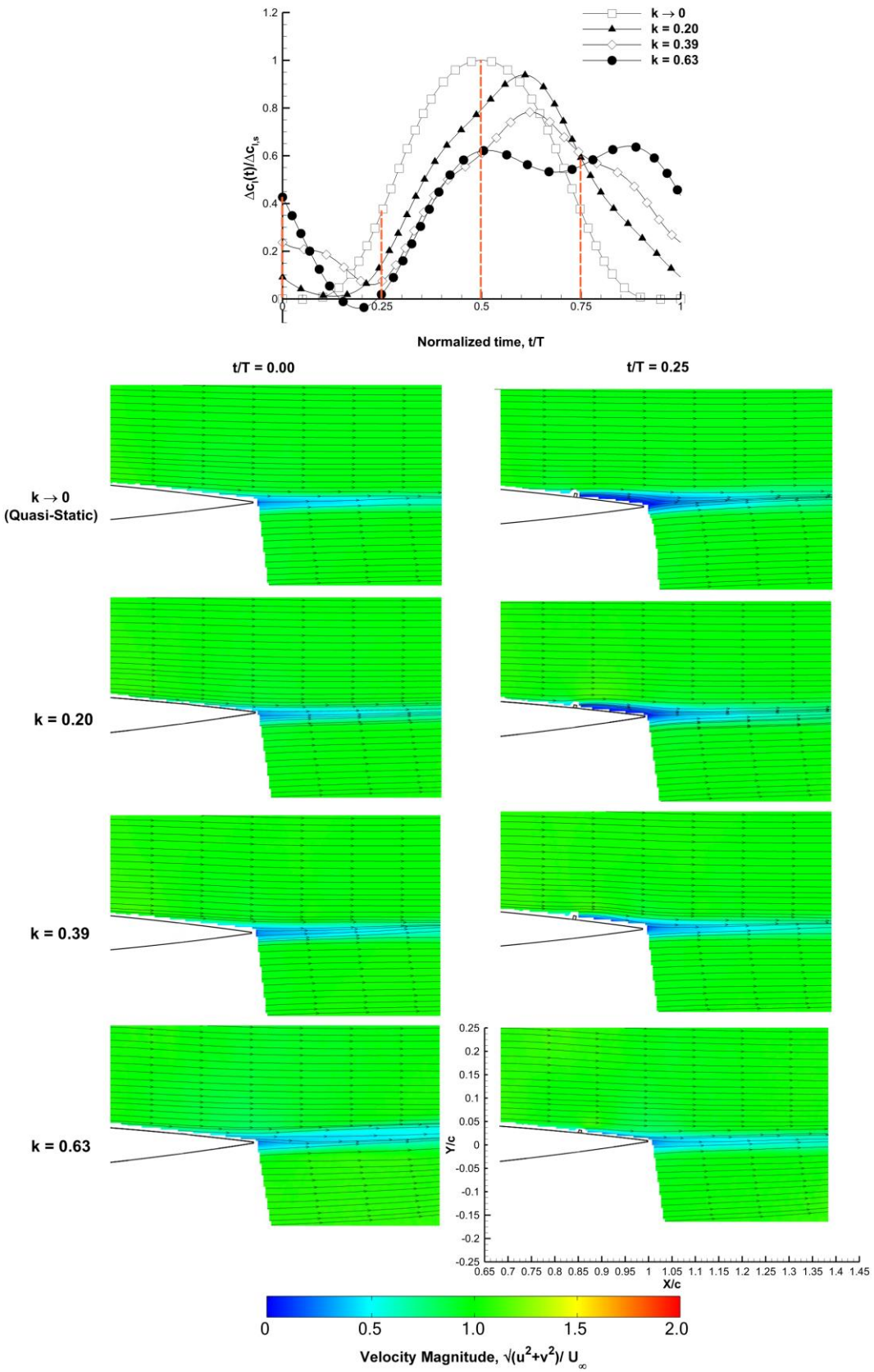

Figure 9: Phase-Averaged flow fields for α = 0°: t/T = 0.00 (1st Column), 0.25 (2nd Column) for reduced frequencies of k → 0, k = 0.20, 0.39 and 0.63.

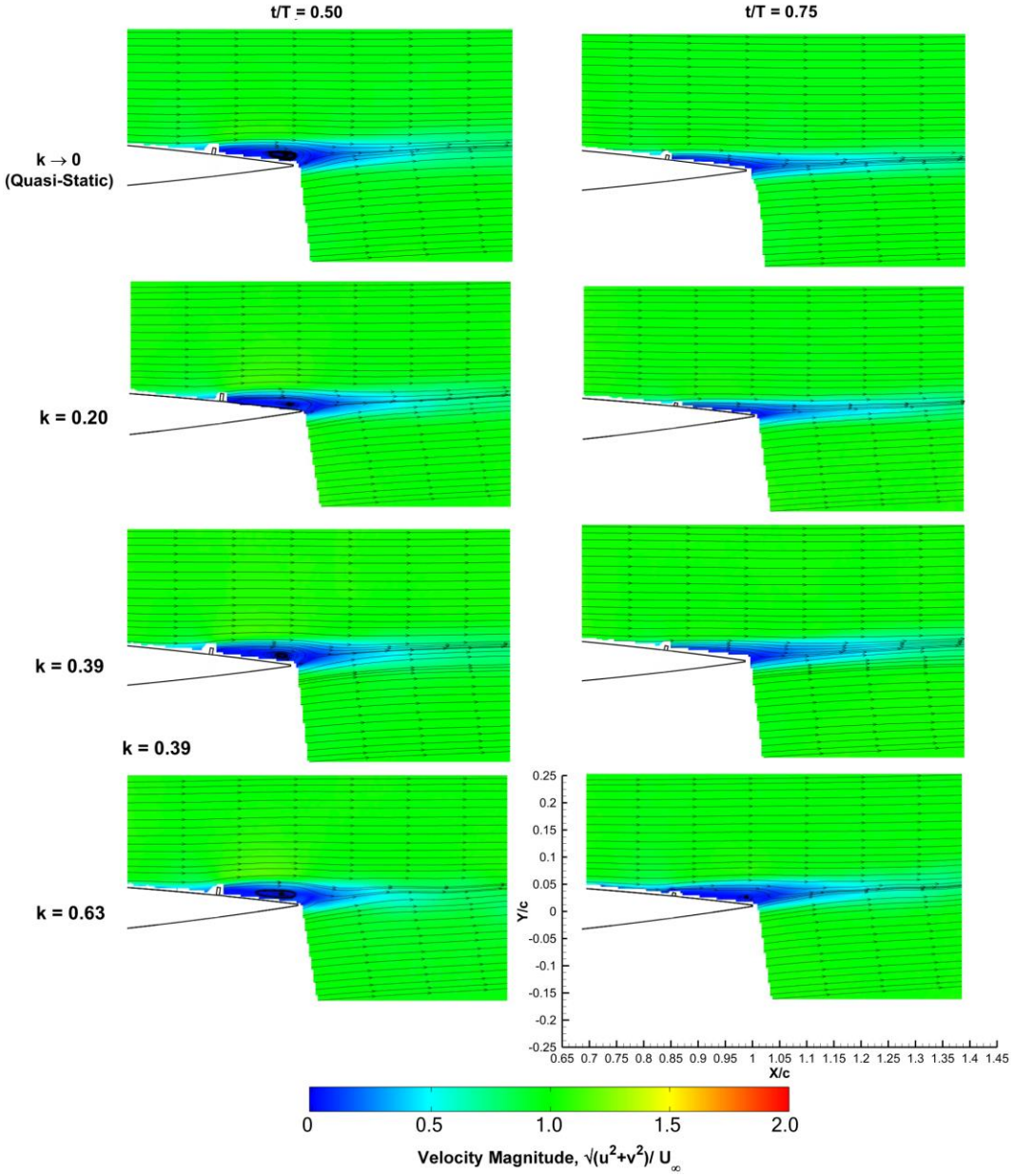

Figure 9 continued: Phase-Averaged flow fields for α = 0°: t/T = 0.50 (1st Column) and 0.75 (2nd Column) for reduced frequencies of k → 0, k = 0.20, 0.39 and 0.63.

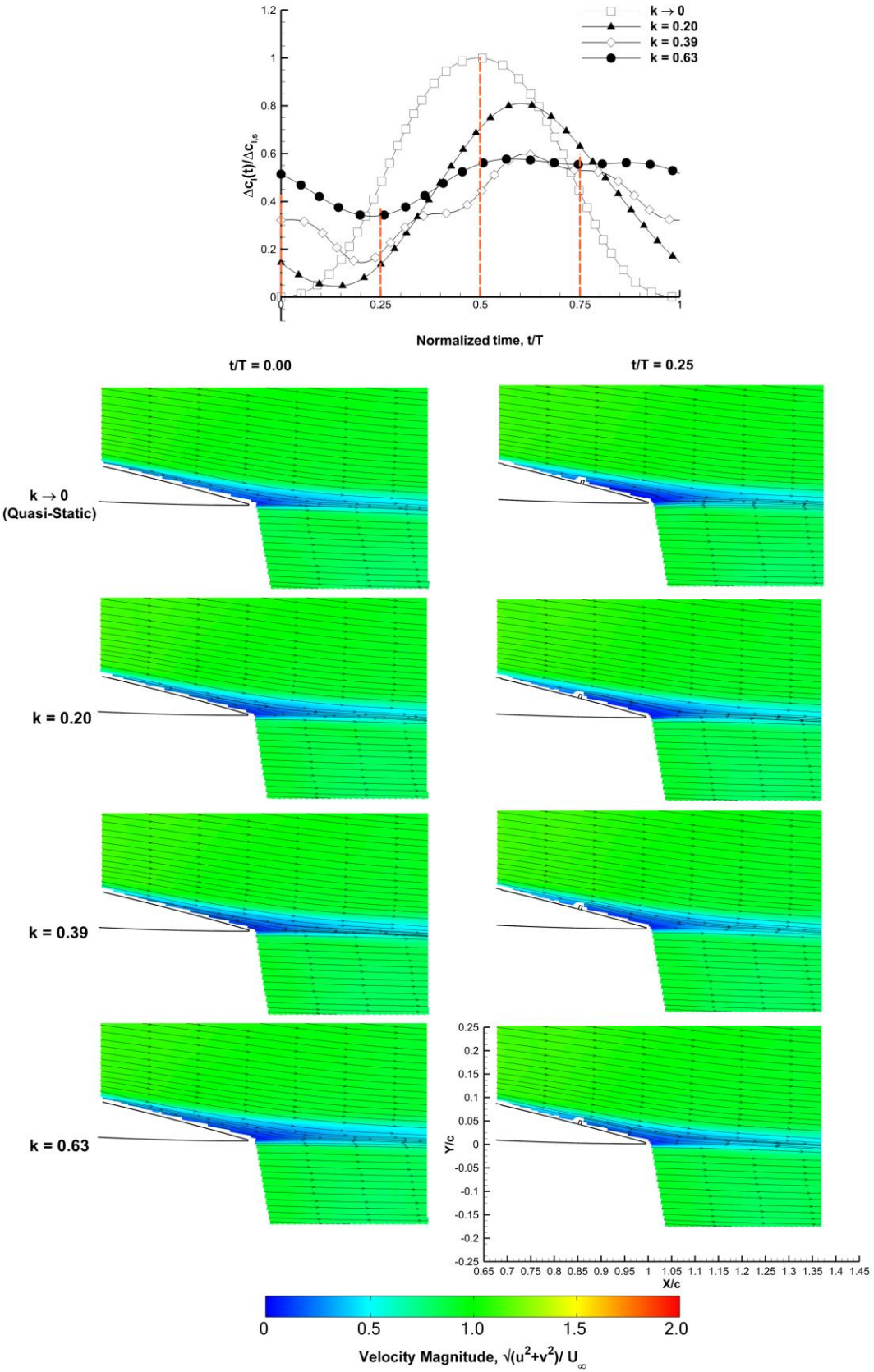

Figure 10: Phase-Averaged flow fields for α = 10°: t/T = 0.00 (1st Column), 0.25 (2nd Column) for reduced frequencies of k → 0, k = 0.20, 0.39 and 0.63.

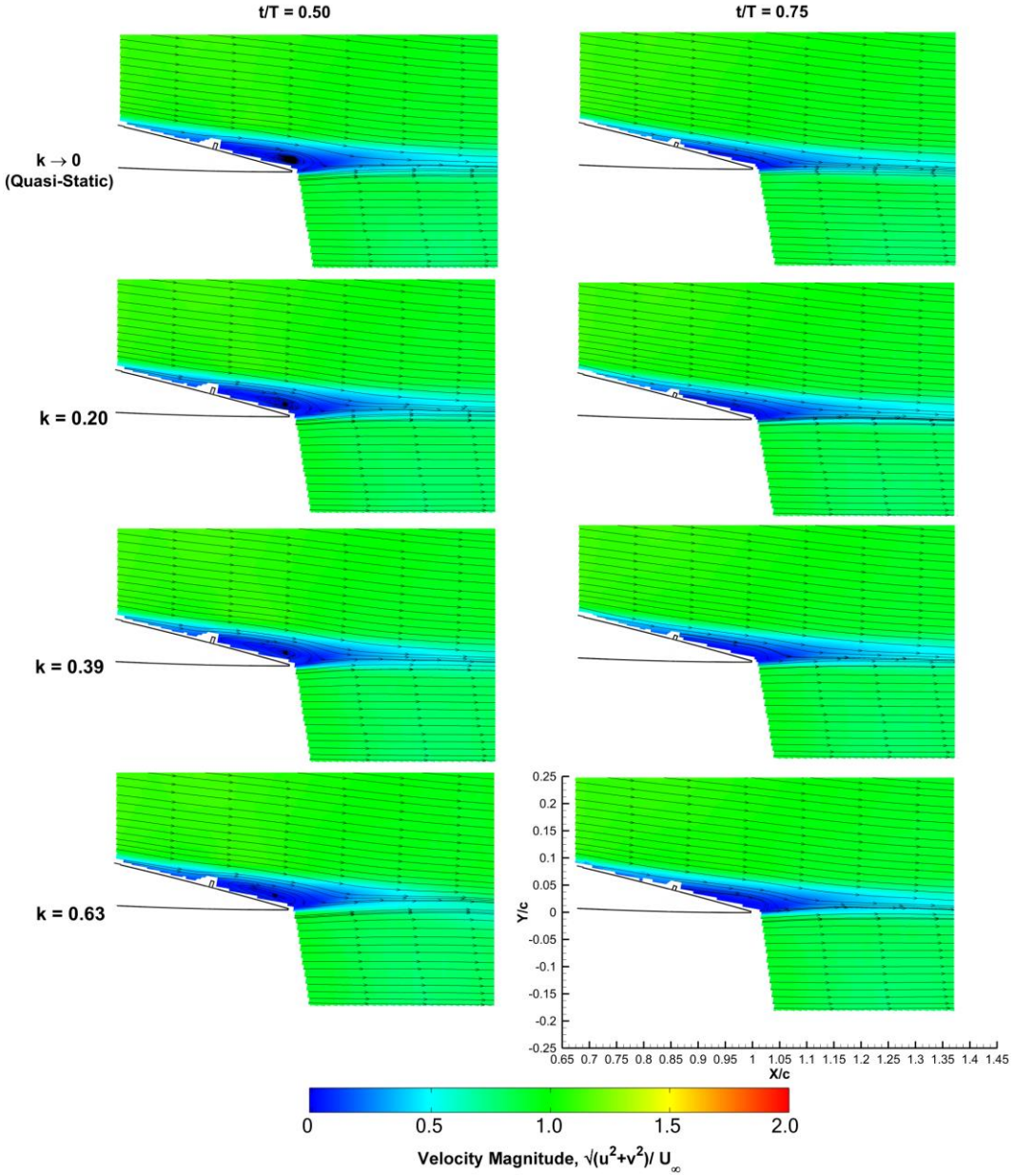

Figure 10 continued: Phase-Averaged flow fields for α = 10°: t/T = 0.50 (1st Column), 0.75 (2nd Column) for reduced frequencies of k → 0, k = 0.20, 0.39 and 0.63.

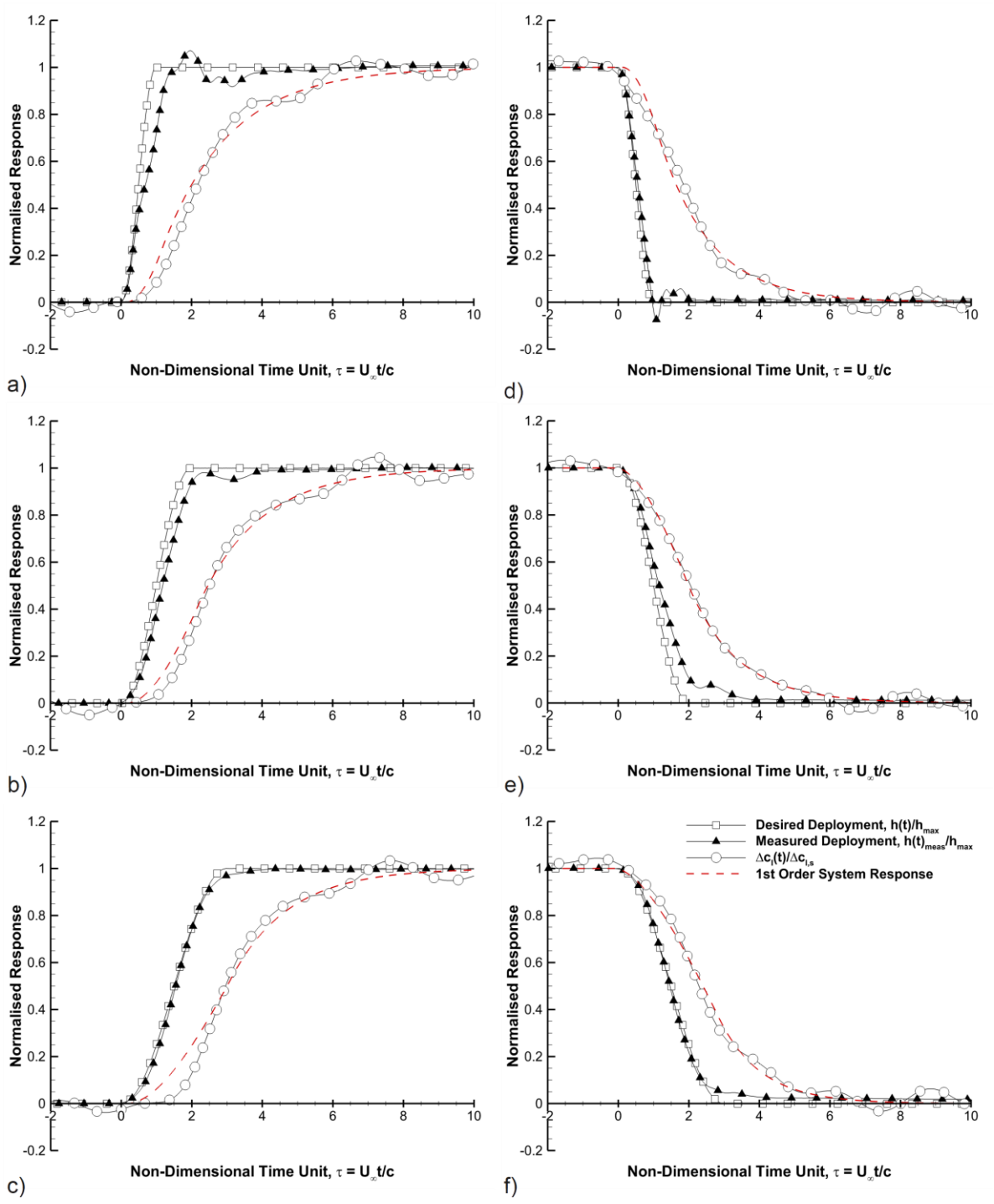

Figure 11: Normalised transient mini-tab motion and lift response for $h_{max}/c = 0.015$ at $\alpha = 0°$ with outward (left column) and inward (right column) directions: (a) & (b) $\tau_{deploy} = 1$, (c) & (d) $\tau_{deploy} = 2$, (e) & (f) $\tau_{deploy} = 3$.

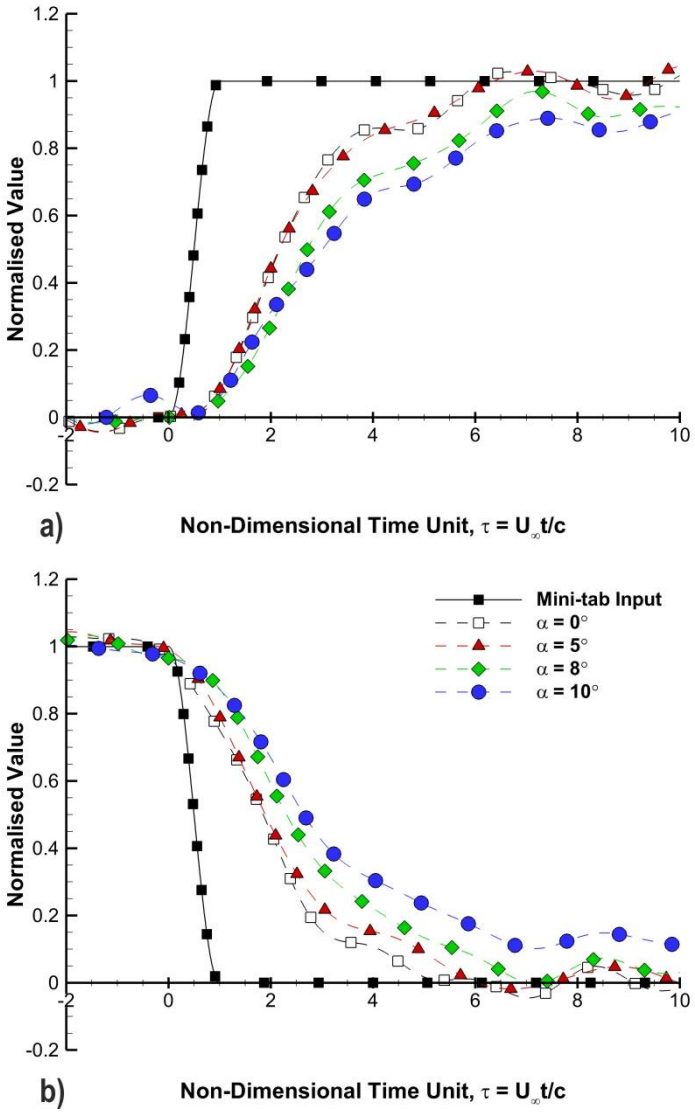

Figure 12: Normalized transient lift response, effect of angle of attack on (a) outward and (b) inward motions for τ_{deploy} = 1 and h_{max}/c = 0.015.

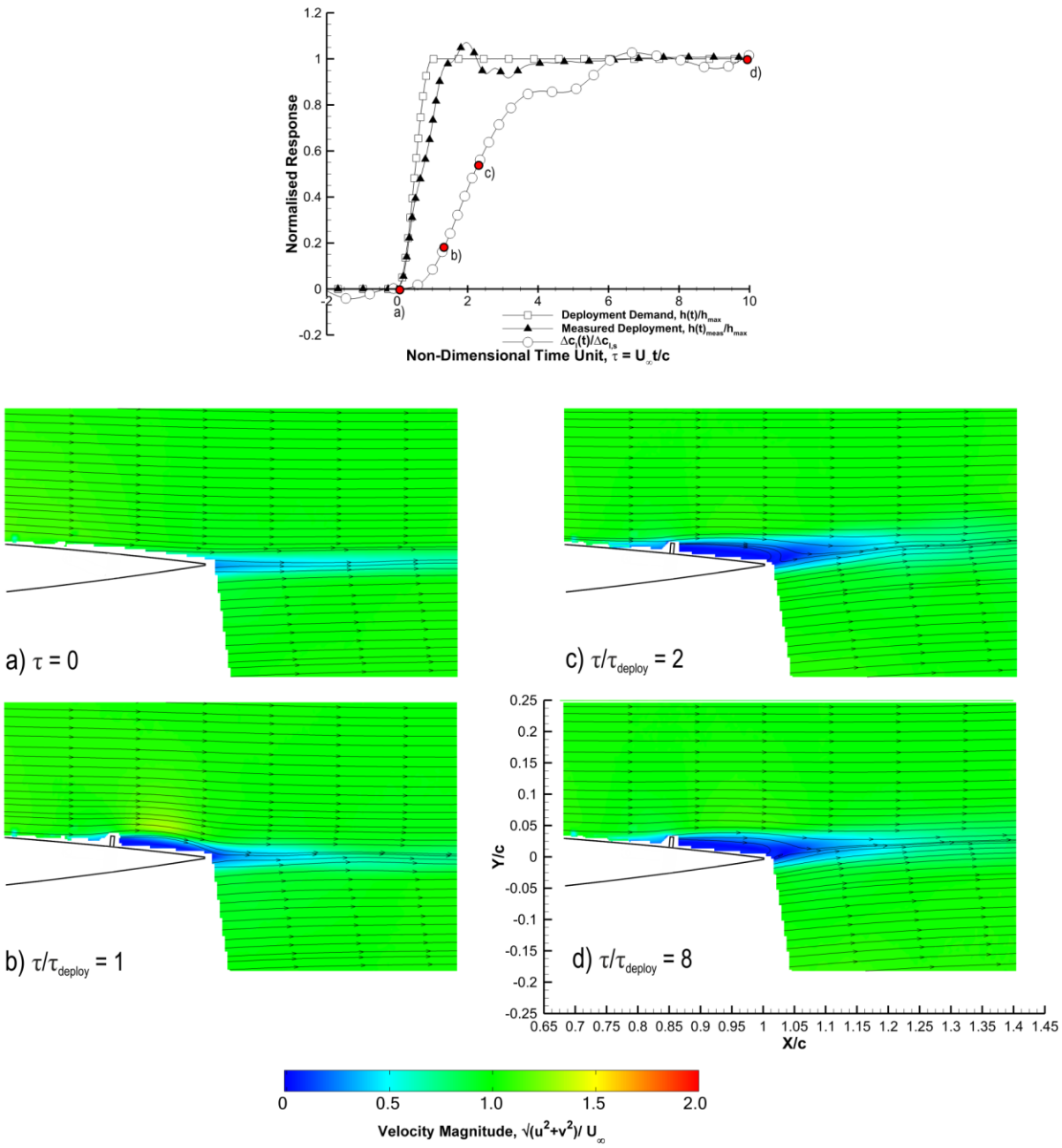

Figure 13: Phase-averaged flow fields for outward mini-tab motion of height, $h_{max}/c = 0.015$ and period, $\tau_{deploy} = 1$. Shown above is the lift response.

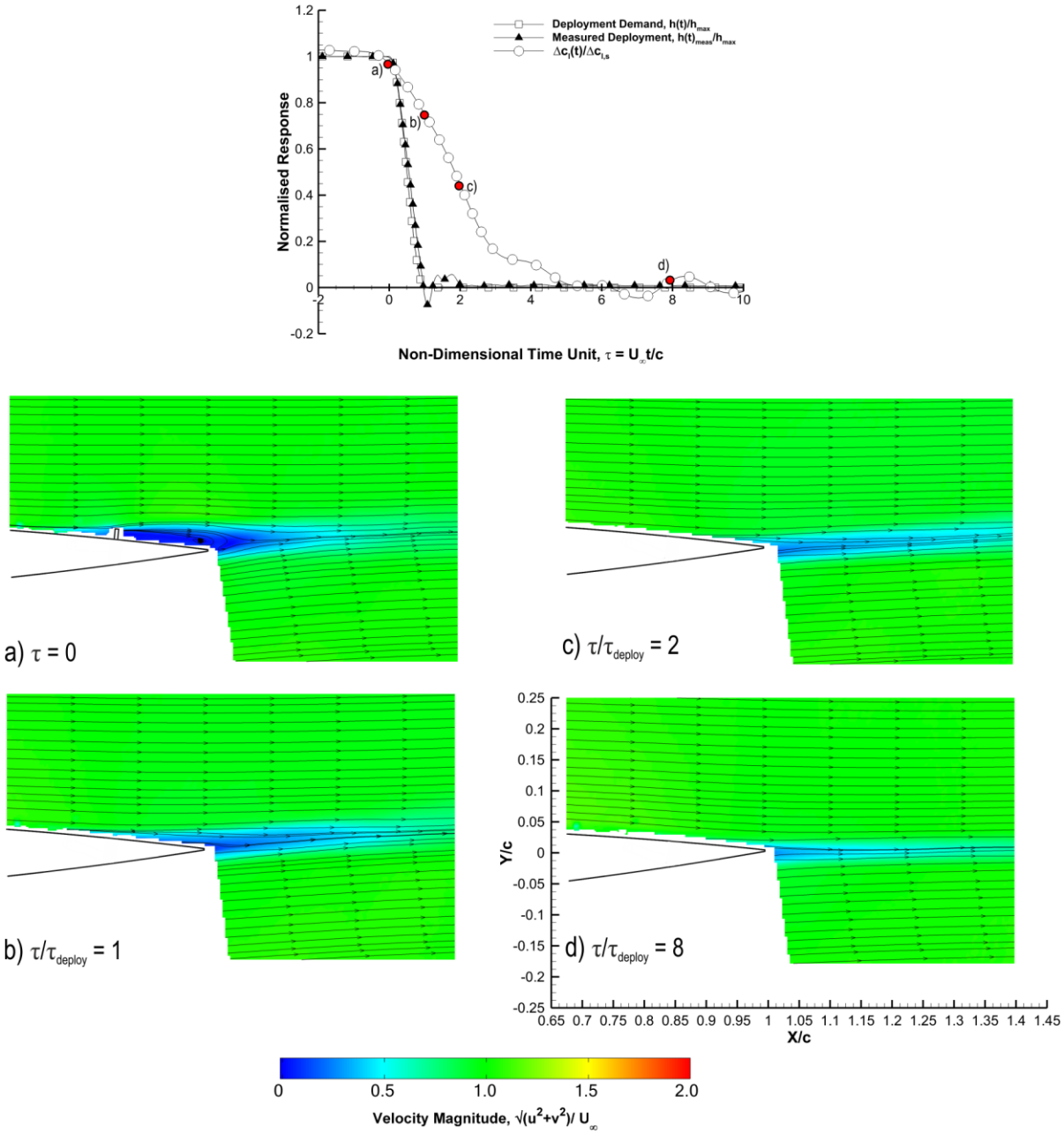

Figure 14: Phase-averaged flow fields and lift response for inward mini-tab motion of height, $h_{max}/c = 0.015$ and period, $\tau_{deploy} = 1$. Shown above is the lift response.

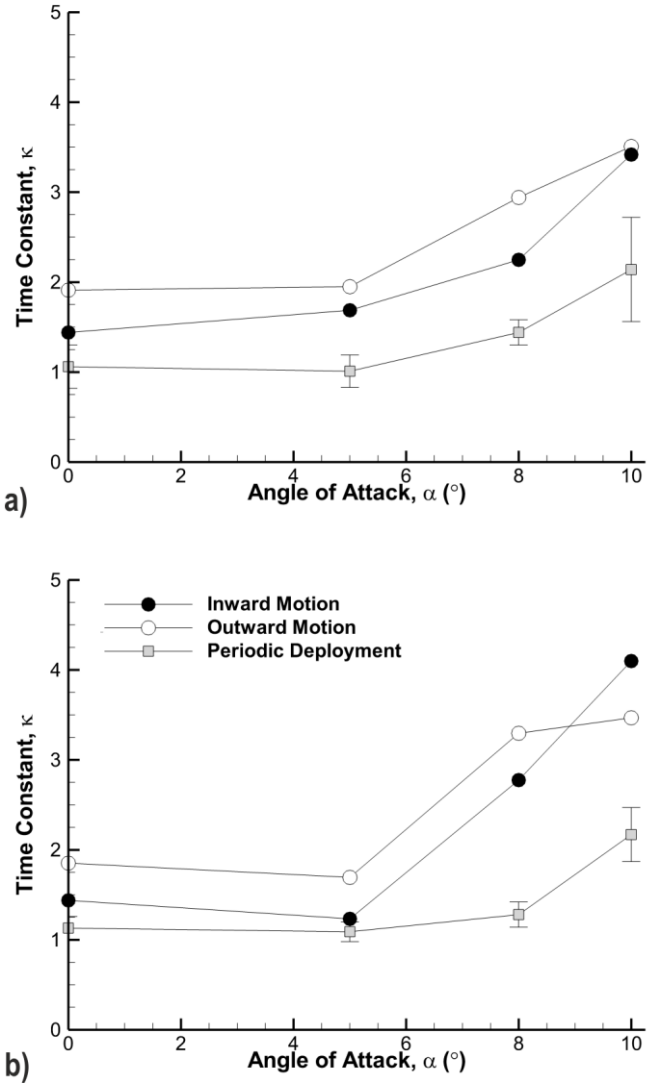

Figure 15: Comparison of time constant, κ values obtained from transient and periodic mini-tab measurements for (a) $h_{max}/c = 0.01$ and (b) $h_{max}/c = 0.015$.

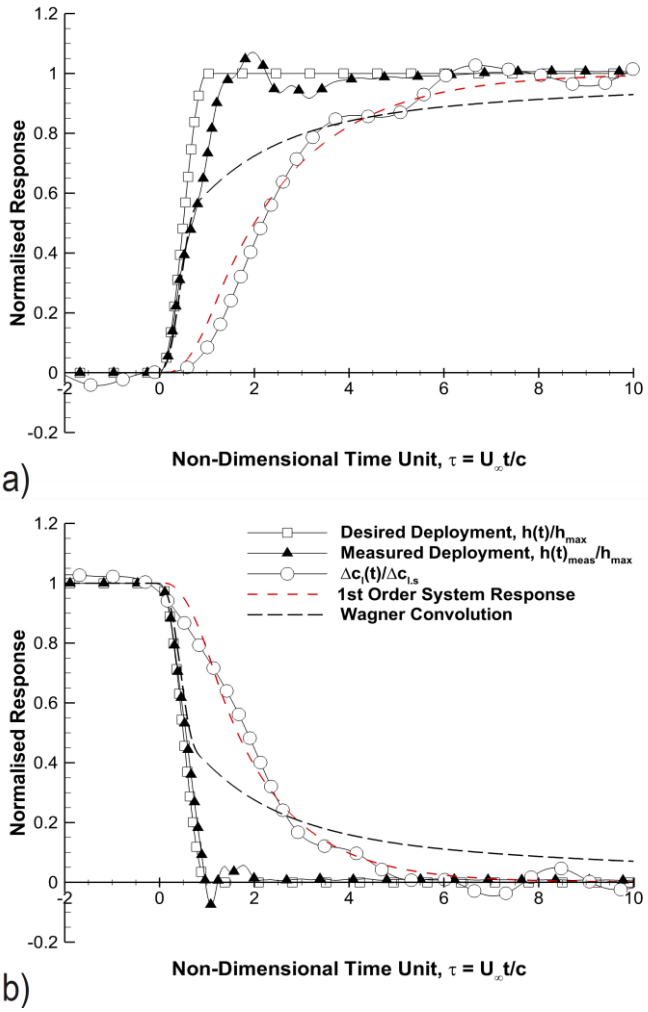

Figure 16: Comparison of (a) outward and (b) inward deployment profiles to a convolution of Wagner's function at α = 0°.